Published OnlineFirst February 16, 2012; DOI:10.1158/0008-5472.CAN-11-3878

mobility shift assay (EMSA) by using radiolabeled synthetic oligoDNA probe containing DNA sequences of ATF/CREB site on the *Angptl2* promoter region (Supplementary Fig. S4C–E). PMA/Ion treatment induced formation of a specific DNA–protein complex (arrowhead in Supplementary Fig. S4C–E), which was inhibited in the presence of unlabeled ATF/CREB competitors (Supplementary Fig. S4C) or by preincubation with an anti-ATF2 antibody (Supplementary Fig. S4D and S4E, lane 4). These findings suggest that ATF2 binds to the *Angptl2* promoter ATF/CREB site. Preincubation with anti-c-Jun antibody reduced DNA–protein complex formation and promoted emergence of a supershifted band (Supplementary Fig. S4E, lane 5, arrow). Preincubation with an anti-NFATc antibody or addition of unlabeled competitor containing the consensus NFATc-binding site partially reduced levels of the DNA–protein complex (Supplementary Fig. S4C and Supplementary Fig. S4E, lane 6). Preincubation with both anti-c-Jun and anti-ATF2 antibodies (Supplementary Fig. S4E, lane 7) or both anti-c-Jun and anti-NFATc antibodies (Supplementary Fig. S4E, lane 8) markedly reduced levels of the DNA–protein complex and the supershifted band. To assay transcription, we cotransfected the F4 construct into H460 cells with expression vectors encoding CA-NFATc, ATF2, c-Jun, c-Fos, or a combination of these vectors and measured luciferase activity (Fig. 2E). Expression of the ATF2/c-Jun combination enhanced *Angptl2* reporter activity relative to controls. CA-NFATc–dependent induction of reporter activity was augmented by c-Jun coexpression. *Angptl2* reporter activity was also markedly increased by coexpression of CA-NFATc/ATF2/c-Jun. However, CA-NFATc/ATF2–dependent or CA-NFATc/c-Jun–dependent induction of reporter activity was not enhanced by c-Fos coexpression. Furthermore, CA-NFATc/ATF2/c-Jun–dependent reporter activity was significantly suppressed when we used an F4 construct containing a mutant ATF/CREB site (Fig. 2F). To determine whether endogenous NFATc, ATF2, and c-Jun bind to the human *Angptl2* promoter, we used chromatin immunoprecipitation (ChIP) assays in H460 cells (Supplementary Fig. S5A). PMA/Ion treatment of cells resulted in increased NFATc and ATF2 binding to the human *Angptl2* promoter region. Previous studies report that c-Jun is highly expressed and activated in NSCLC cell lines (23, 24). c-Jun binding to the human *Angptl2* promoter region was observed in PMA/Ion-untreated H460 cells, whereas that binding level was unchanged in PMA/Ion-treated cells (Supplementary Fig. S5A). Taken together, these observations show that NFATc plays an important role in *Angptl2* induction and that an ATF2/c-Jun complex likely enhances NFATc-dependent *Angptl2* induction through the ATF/CREB site.

NFATc2 knockdown decreases *Angptl2* expression in tumor cells

The NCI-H460-LNM35 (LNM35) line was established by *in vivo* selection as a highly metastatic subline of the human large cell carcinoma of the lung, NCI-H460 (15). We found that that severe immunodeficient Jak3-deficient NOD-SCID (NOJ) mice (25) subcutaneously injected with LNM35 cells showed shortened survival periods due to high frequency metastasis to lung and lymph nodes compared with mice injected with H460 cells (Supplementary Fig. S6). Interestingly, *Angptl2* mRNA is more abundant in cultured LNM35 cells than in H460 cells (Fig. 3A). We found that NFATc1, NFATc2, and NFATc3 increased *Angptl2* promoter activity in the H460 cells (Supplementary Fig. S5B and S5C). *NFATc2* expression in LNM35 cells was significantly higher than that seen in H460 cells, whereas expression of NFATc1, NFATc3, and NFATc4 was equivalent in both lines (Fig. 3B). NFATc2 protein levels were also markedly increased in LNM35 cells, but ATF2 and c-Jun protein levels were equivalent (Fig. 3C). To examine whether NFATc2 is required for *Angptl2* expression in LNM35 cells, we established 2 LNM35 cell lines each stably expressing a different miR RNA interference (RNAi) expression vector designed to knockdown *NFATc2* (LNM35/miNFATc2-1 and LNM35/miNFATc2-2; Fig. 3D). *Angptl2* expression levels in both lines were significantly decreased compared with control cells and comparable with those seen in H460 cells (Fig. 3E). Invasive activity of LNM35/miNFATc2 cells was decreased compared with controls (Supplementary Fig. S7). These observations suggest that NFATc2 is important for *Angptl2* expression and acquisition of tumor invasivity.

Angptl2-expressing tumor cells contribute to increased tumor metastasis

As indicated in Fig. 1 and Supplementary Fig. S2, ANGPTL2-positive tumor cells exhibit higher metastatic capacity than ANGPTL2-negative cells. We therefore generated 2 independent H460 lines constitutively expressing *Angptl2* (H460/Angptl2-1 and -2) and an H460 line expressing a control vector (H460/Cont; Fig. 4A). Although no differences were observed in *in vitro* growth among all 3 lines (Supplementary Fig. S8A), *in vitro* invasive capacity of the 2 H460/Angptl2 lines was significantly greater than that seen in H460/Cont (Fig. 4B). We next analyzed tumor development after subcutaneous injection of either the 3 lines into mice. Despite equivalence in *in vivo* tumor growth observed among the 2 H460/Angptl2 lines and H460/Cont (Supplementary Fig. S8B and S8C), lung metastasis was more severe in mice bearing H460/Angptl2-1 tumors than in H460/Cont controls (Fig. 4C and D). Tumor angiogenesis was also increased in mice bearing H460/Angptl2-1 compared with H460/Cont cells (Supplementary Fig. S8D and S8E), a finding consistent with our recent report (5). Finally, the survival period of mice bearing H460/Angptl2 tumors was significantly shortened compared with H460/Cont mice (Fig. 4E).

Angptl2 increases tumor cell motility by activating Rac

Time-lapse imaging indicated that H460/Angptl2-1 cells are significantly more motile than are H460/Cont cells (Fig. 5A and B, Supplementary Movie S1 and S2). Histologic analysis indicated that H460/Angptl2-1 cells exhibit a polarized morphology associated with motility, as evidenced by formation of actin-rich lamellipodial protrusions and assembly of paxillin-marked focal complexes at the leading edge, whereas H460/Cont cells displayed nonpolarized morphology with uniform distribution of F-actin and paxillin at the cell periphery (Fig. 5C and D). Because activation of Rac1, a Rho family GTPase, at a cell's leading edge is required to form lamellipodial protrusions

Published OnlineFirst February 16, 2012; DOI:10.1158/0008-5472.CAN-11-3878

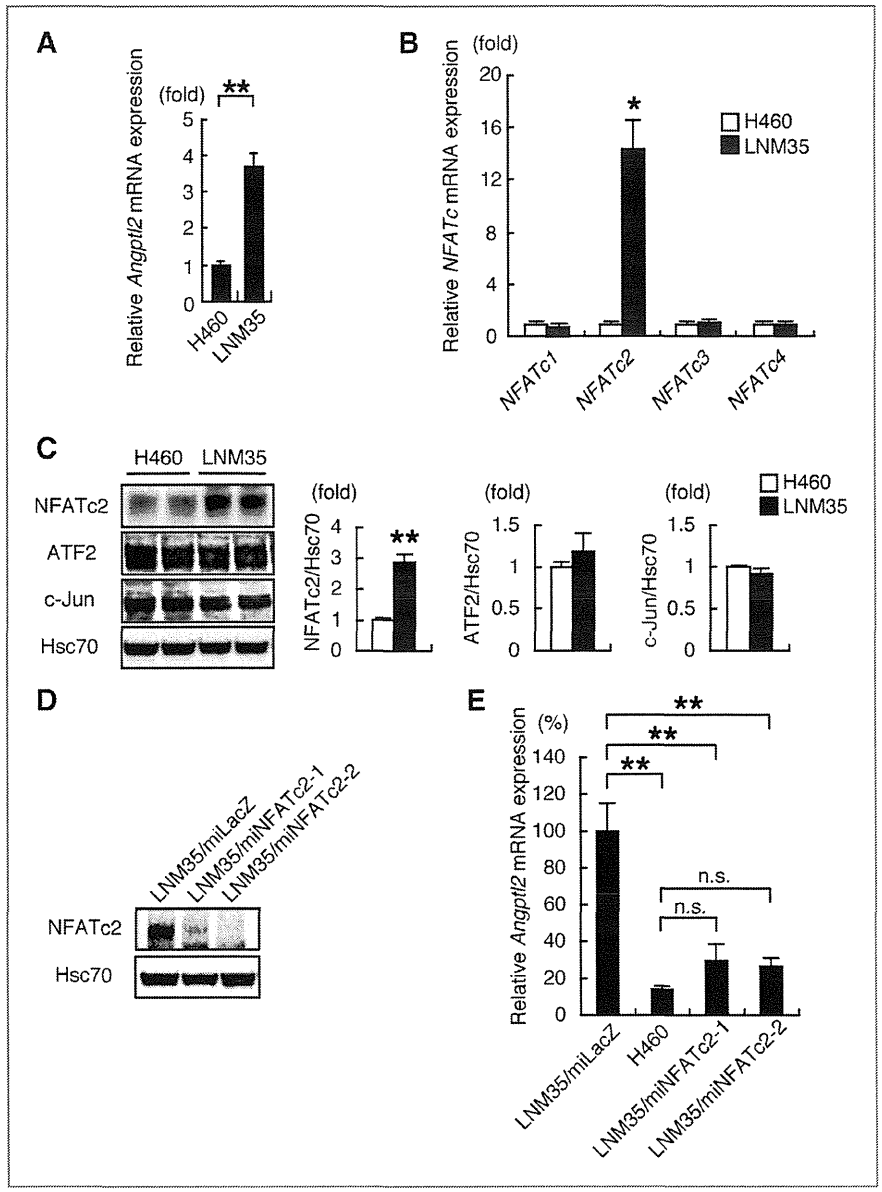

Figure 3. *NFATc2* knockdown decreases *Angptl2* expression. A, comparison of relative *Angptl2* mRNA levels between H460 and LNM35 cells. Data from H460 were set at 1. B, comparison of relative *NFATc* mRNA levels between H460 and LNM35 cells. Data from H460 were set at 1. C, left, representative image of immunoblotting analysis of NFATc2, ATF2, and c-Jun protein levels in H460 and LNM35 cells. Hsc70 served as control. Right, quantitative protein levels of NFATc2, ATF2, and c-Jun relative to Hsc70. Data from H460 were set at 1, respectively. D, representative image of immunoblotting of NFATc2 protein levels in indicated cells. E, comparison of *Angptl2* mRNA levels among indicated cells. Data from LNM35/miLacZ were set to 100%. All experiments were carried out more than 3 times. Error bars show SEM. *, $P < 0.05$; **, $P < 0.01$; n.s., no statistical difference.

required for cell migration (26), we asked whether ANGPTL2 activates Rac1 using a FRET probe to visualize Rac1 activation in H460/Angptl2-1 and H460/Cont cells. Rac1 was potently activated at the leading edge of migrating H460/Angptl2-1 cells, whereas no polarized Rac1 activation was observed in H460/Cont cells (Fig. 5E, Supplementary Movie S3 and S4). Collectively, these data suggest that tumor cell–derived ANGPTL2 promotes actin reorganization and accelerates cell migration via Rac1 in an autocrine and/or paracrine manner.

Angptl2 knockdown suppresses tumor metastasis

Because LNM35 cells express *Angptl2* abundantly and exhibit high metastatic capacity due to enhanced polarized morphology compared with H460 cells (Fig. 3, Supplementary Figs. S6 and S9), we examined the effect of *Angptl2* knockdown in LNM35 cells. Of 4 candidate miR RNAi expression vectors (miAngptl2-a, -b, -c, and -d) recommended by the Invitrogen BLOCK-iT miR RNAi System, miAngptl2-b significantly decreased *Angptl2* expression compared with a LNM35 line harboring *LacZ* knockdown (LNM35/miLacZ) used as a control (Supplementary Fig. S10). We therefore generated 2 independent *Angptl2* knockdown lines: LNM35/miAngptl2-b1 and -b2 (Supplementary Fig. S11A). *In vitro* invasive ability was significantly decreased in both lines compared with LNM35/miLacZ cells, whereas no differences in *in vitro* cell growth were observed among knockdown and control lines (Supplementary

Published OnlineFirst February 16, 2012; DOI:10.1158/0008-5472.CAN-11-3878

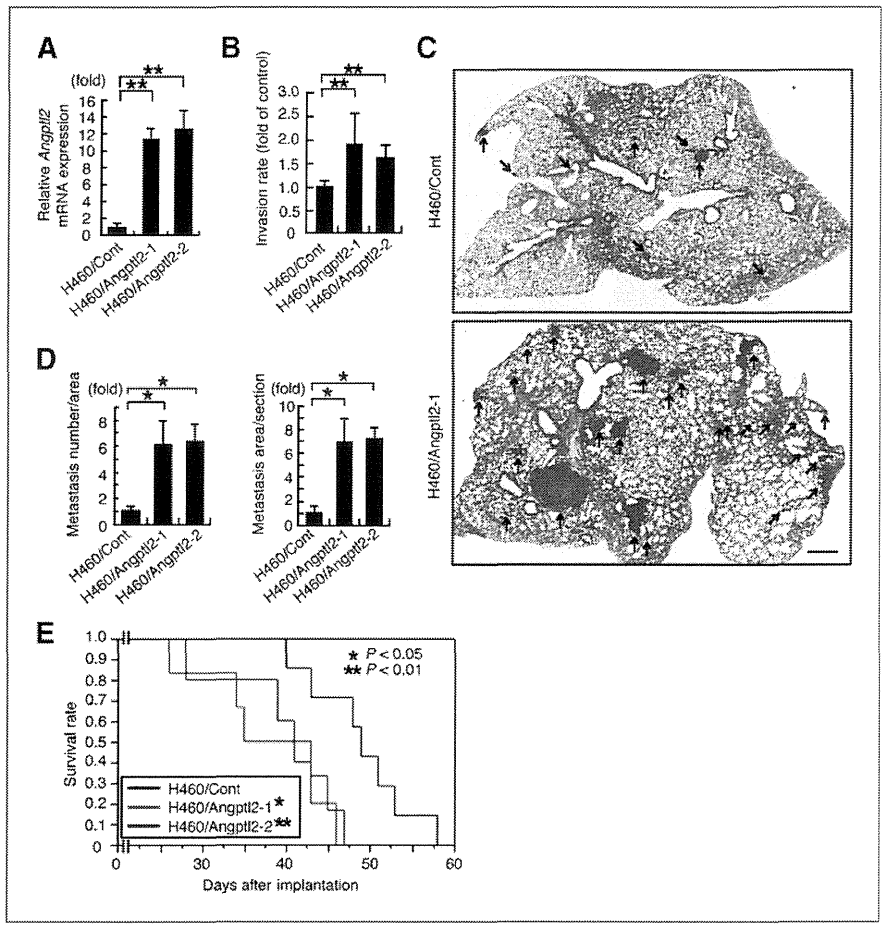

Figure 4. Increased *Angptl2* expression in tumor cells enhances tumor metastasis. A, relative *Angptl2* mRNA levels among indicated cells. Data from H460/Cont were set at 1. B, relative invasive capacity of indicated cells. Data from H460/Cont were set at 1. C, representative hematoxylin and eosin (H&E)-stained images of tumor metastasis (arrows) to lung 4 weeks after injection with H460/Cont (top) or H460/Angptl2-1 (bottom) cells. Scale bar, 200 μm. D, quantitative analysis of (C) for severity of metastasis ($n = 12$). Relative number (left) and area (right) of tumor metastases in lung tissue among indicated cells. Data from H460/Cont were set at 1. E, Kaplan–Meier survival curves of mice bearing tumors derived from H460/Cont . ($n = 10$), H460/Angptl2-1 ($n = 10$), and H460/Angptl2-2 ($n = 7$) cells. All experiments were carried out more than 3 times. Error bars show SD. *, $P < 0.05$; **, $P < 0.01$.

Fig. S11B and S11C). In addition, both knockdown lines displayed less polarized morphology and more uniform distribution of F-actin and paxillin compared with LNM35/miLacZ cells (Supplementary Fig. S12). Mice bearing both *Angptl2* knockdown lines showed no significant difference in tumor growth but exhibited markedly decreased lung metastases compared with mice bearing LNM35/miLacZ cells (Supplementary Fig. S11D–G). Survival times were also extended in mice injected with knockdown versus control lines (Supplementary Fig. S11H). These results suggest that tumor cell–derived ANGPTL2 increases metastasis and that decreased ANGPTL2 expression in tumor cells can attenuate that effect.

Tumor cell–derived ANGPTL2 enhances lung metastasis in mice bearing breast cancer cells

To investigate whether tumor cell–derived ANGPTL2 enhances metastasis in other cancer types, we examined ANGPTL2 expression and function in the human breast cancer lines T47D, MDA-MB453, and MDA-MB231. Only MDA-MB231, which shows an aggressive metastatic phenotype (27), abundantly expressed and secreted ANGPTL2 (Fig. 6A and B). MDA-MB231 cells also expressed NFATc2, ATF2, and c-Jun (Fig. 6A), whereas MDA-MB231 cells stably expressing *NFATc2* RNAi (MB231/miNFATc2) showed significantly decreased *Angptl2* mRNA and protein secretion compared with control MB231/miLacZ cells (Fig. 6C, Supplementary Fig. S13A and S13B). We established 2 independent MDA-MB231 lines expressing miR RNAi (miAngptl2-b) to knockdown *Angptl2* (MB231/miAngptl2-b1 and -2) and a control LacZ RNAi line (MB231/miLacZ). In knockdown lines cellular *Angptl2* mRNA levels and levels of ANGPTL2 protein in the culture medium were significantly decreased compared with those seen in controls (Supplementary Fig. S13C). All 3 lines showed similar *in vitro* growth (Supplementary Fig. S13D), whereas *in vitro* invasive capacity was significantly decreased in knockdown compared with control cells (Supplementary Fig. S13E).

Next, we carried out *in vivo* xenograft tumor experiments by implanting various lines of MDA-MB231 cells into the mouse mammary fat pad. For imaging purposes, we induced a luciferase expression vector into MB231/miAngptl2-b1 and -2 and control MB231/miLacZ cells to create MB231/miAngptl2-b1/luc, MB231/miAngptl2-b2/luc, and MB231/miLacZ/luc, respectively. No difference in *in vivo* tumor growth was seen among the 3 lines (Fig. 6D, Supplementary Fig. S13F). In contrast, lung metastasis was observed in mice bearing MB231/miLacZ/luc 5 weeks after tumor implantation,

Published OnlineFirst February 16, 2012; DOI:10.1158/0008-5472.CAN-11-3878

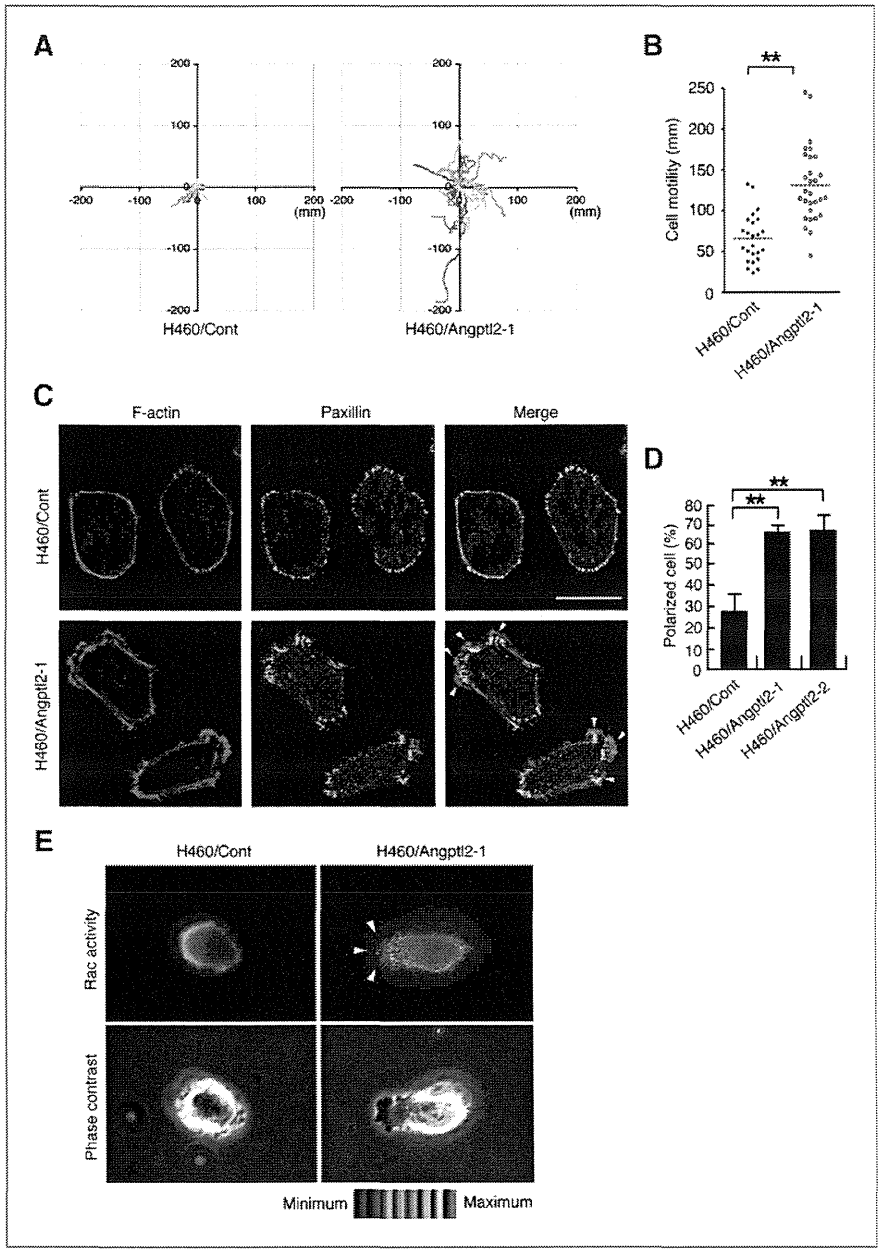

Figure 5. *Angptl2* expression positively correlates with cell motility. A, migration tracks of 20 H460/Cont (left) and H460/Angptl2-1 (right) cells monitored for 5 hours. B, quantitative comparison of the extent of movement of individual tumor cells. C, representative fluorescent immunostaining images for F-actin (left) and paxillin (middle) of H460/Cont (top) and H460/Angptl2-1 (bottom) cells. Arrowheads indicate the leading edge. Scale bar, 20 μm. D, quantitative analysis of polarized cells. E, FRET imaging of Rac activity. Arrowheads indicate site of activated Rac.

whereas fewer metastatic sites at the same time point was observed in mice bearing MB231/miAngptl2-b1/luc. To see equivalent lung metastasis after tumor implantation in mice bearing MB231/miAngptl2-b1/luc required 8 weeks (Fig. 6D). Immunohistochemistry with an anti-CD44 antibody, which detects MDA-MB231 cells (27), showed statistically significant decreases in lung colonization of MB231/miAngptl2-b1 compared with MB231/miLacZ cells (Fig. 6E and F). Moreover, decreased tumor angiogenesis was observed in mice bearing MB231/miAngptl2-b1 compared with MB231/miLacZ cells (Supplementary Fig. S14). Mice bearing the 2 MB231/miAngptl2 lines also showed prolonged survival periods compared with controls (Fig. 6G), suggesting that tumor cell–derived ANGPTL2 accelerates tumor metastasis in breast as well as in lung cancer.

Discussion

Here, we show that tumor cells expressing ANGPTL2 exhibit high metastatic potential through acquisition of invasive and high cell motility phenotypes in an autocrine/paracrine manner. We also showed that NFATc, ATF2, and c-Jun induce

Published OnlineFirst February 16, 2012; DOI:10.1158/0008-5472.CAN-11-3878

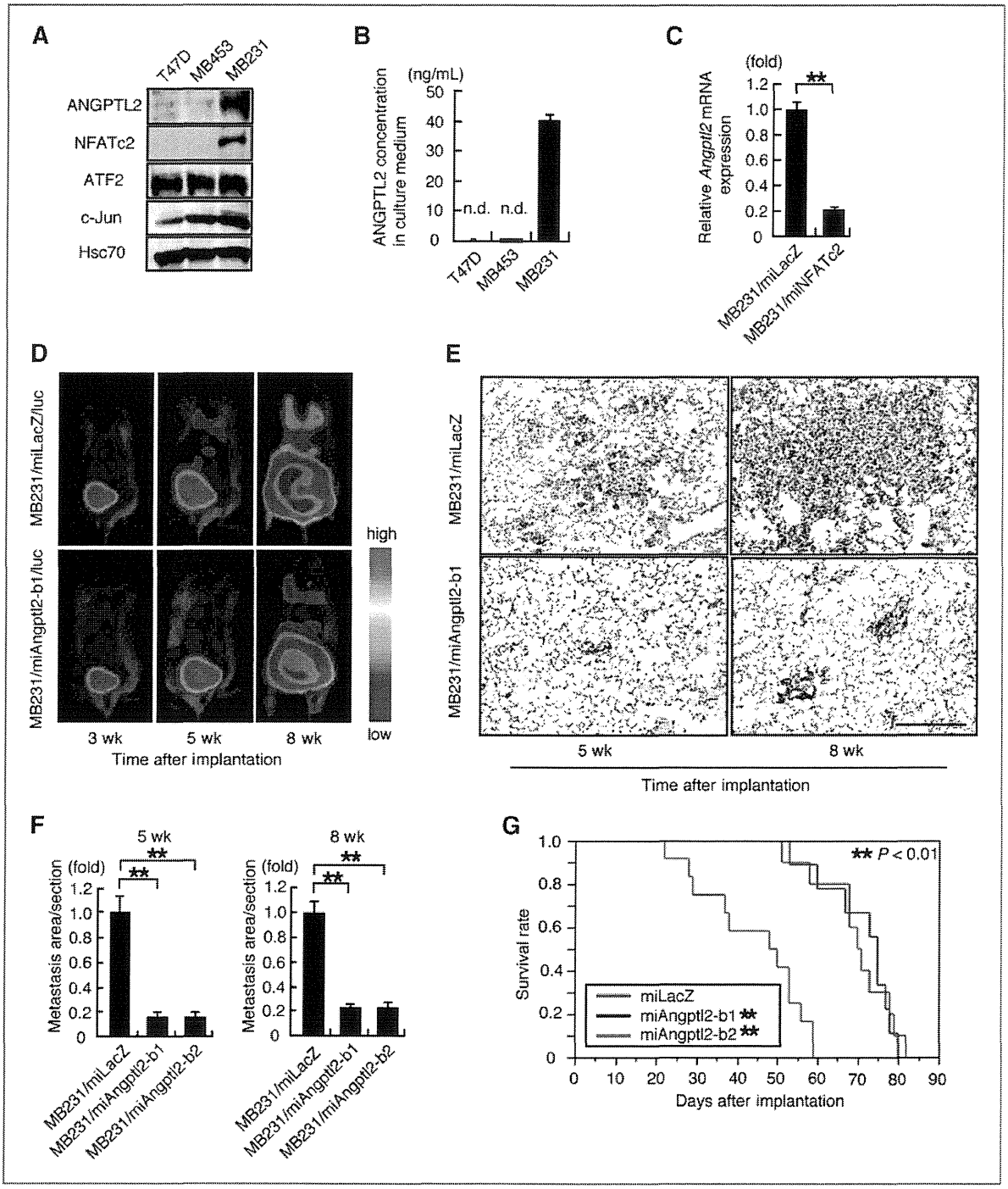

Figure 6. *Angptl2* knockdown in breast cancer cells reduces metastatic capacity. A, representative image of immunoblotting of ANGPTL2, NFATc2, ATF2, and c-Jun protein levels in indicated cells. B, comparison of ANGPTL2 levels in culture medium of indicated cells. n.d., not detected. C, comparison of relative *Angptl2* mRNA levels in indicated cells. Data from MB231/miLacZ were set at 1. D, representative bioluminescence images of mice bearing MB231/miLacZ/luc or MB231/miAngptl2-b1/luc cells. Images were taken at indicated time points after xenografting ($n = 12$). E, representative microscopic images of tumor cells metastasized to lung, as recognized by anti-CD44 immunostaining, 5 (left) and 8 (right) weeks after implantation with MB231/miLacZ (top) or MB231/miAngptl2-b1 (bottom) cells. Scale bar, 500 μm. F, quantitative analysis of (E) for severity of metastasis ($n = 10$). Relative area of tumor metastases in lung among the 3 cell lines at 5 (left) and 8 (right) weeks is shown. Data from MB231/miLacZ were set at 1. G, Kaplan–Meier survival curves of mice bearing tumors derived from MB231/miLacZ ($n = 12$), MB231/miAngptl2-b1 ($n = 10$), or MB231/miAngptl2-b2 ($n = 10$) cells. All experiments were carried out at least 3 times. Error bars show SD. **, $P < 0.01$.

Published OnlineFirst February 16, 2012; DOI:10.1158/0008-5472.CAN-11-3878

Angptl2 expression, providing a mechanism for tumor cell ANGPTL2 induction. These findings are consistent with previous reports showing that activation of ATF/CREB family proteins and/or the calcineurin/NFATc pathway occurs in aggressively advanced tumors (6, 19, 28, 29).

We have reported that obese adipose tissue–related endoplasmic reticulum (ER) stress increases ANGPTL2 secretion or expression in adipocytes (13). ER stress is easily induced by stresses such as hypoxia, oxidative stress, hypoglycemia, and viral infection, all commonly observed in primary tumor microenvironment (30). We found that *Angptl2* mRNA levels in tumor cells were significantly increased under hypoxia and under nutrition (Supplementary Fig. S15A). In addition, increased ANGPTL2 expression was detected in tumor cells in hypoxic regions (Supplementary Fig. S15B), suggesting that tumor microenvironmental factors, such as hypoxia and/or under nutrition, induce ANGPTL2 expression in tumor cells. Cytoplasmic calcium concentrations increase due to ER stress–dependent calcium release from the ER (31) and activate the serine/threonine phosphatase calcineurin, which in turn dephosphorylates NFATc proteins and triggers their nuclear accumulation (32). NFATc function has been extensively studied in the immune system, but there is increased interest in NFATc activity in cancer (6). We speculate that tumor cell autonomous responses to the microenvironment, such as activation of the ER stress/calcineurin/NFATc pathway and/or ATF/CREB family proteins, induce *Angptl2* expression in tumor cells, resulting in acquisition of aggressively metastatic tumor phenotypes.

Interestingly, a recent report suggests that ANGPTL2 might function in tumor refractoriness to anti-VEGF therapy (33). On the other hand, VEGF reportedly activates an inhibitor of calcineurin/NFATc signaling, namely, the Down syndrome critical region gene 1 (DSCR1; refs. 34, 35). Taken together with these 2 reports, our findings suggest that in tumors refractory to anti-VEGF treatment, suppression of VEGF signaling may inactivate DSCR1 and thereby activate NFATc, resulting in increased ANGPTL2 expression and ANGPTL2-dependent tumor progression. Overall, we propose that the tumor microenvironment activates NFATc and ATF/CREB family proteins in tumor cells, resulting in ANGPTL2 induction and subsequent tumor metastasis.

On the basis of the results of EMSA and ChIP assays, we suggested that NFATc, ATF2, and c-Jun form a complex and bind to the *Angptl2* promoter region in PMA/Ion-treated H460 cells. CA-NFATc–dependent induction of the *Angptl2* reporter activity was augmented by c-Jun coexpression, and the augmentation was significantly enhanced by ATF2 coexpression. In contrast, ATF2 alone did not induce the *Angptl2* reporter activity. Therefore, we consider that ATF2 would be important to form a complex with NFATc and c-Jun to induce the *Angptl2* reporter activity.

We previously reported that ANGPTL2 increases angiogenesis through Rac activation in endothelial cells (13). Consistently, here we found that tumor cell–derived ANGPTL2 increases tumor angiogenesis. Interestingly, we also found that ANGPTL2 directly accelerates tumor cell motility through Rac activation in tumor cells. We observed that EMT occurs prominently in *Angptl2*-expressing human lung cancer cells (Supplementary Figs. S16 and S17) as well as in a chemically induced mouse SCC expressing *Angptl2* (5). Two types of tumor cell movements have been described: a Rac-dependent mesenchymal mode and a Rho-dependent amoeboid mode (36), suggesting that ANGPTL2 induces cell motility in the mesenchymal mode. Because the EMT in tumor cells decreases intercellular adhesion, cell motility is enhanced, resulting in tumor invasion and metastasis. Thus, ANGPTL2 might be a key factor in increasing cell motility in tumor cells with mesenchymal characteristics.

Overall, we show that tumor cell–derived ANGPTL2 accelerates tumor metastasis through increasing tumor cell migration in an autocrine/paracrine manner in addition to enhancing tumor angiogenesis, as described here and reported previously (5; Supplementary Fig. S18). On the basis of these findings, we propose that ANGPTL2 regulates tumor metastasis in human lung and breast cancer. These studies could form the basis of new therapeutic strategies to antagonize tumor metastasis.

Disclosure of Potential Conflicts of Interest

No potential conflicts of interest were disclosed.

Authors' Contributions

Conception and design: M. Endo, M. Nakano, T. Kadomatsu, Y. Oike

Development of methodology: M. Endo, M. Nakano, T. Kadomatsu, K. Miyata, T. Ito, S. Okada, Y. Oike

Acquisition of data (provided animals, acquired and managed patients, provided facilities, etc.): M. Endo, M. Nakano, T. Kadomatsu, S. Fukuhara, H. Kuroda, S. Mikami, T. Hato, J. Aoi, H. Horiguchi, K. Miyata, M. Harada, H. Horio, T. Hishima, H. Nomori, T. Ito, S. Okada, N. Mochizuki, Y. Oike

Analysis and interpretation of data (e.g., statistical analysis, biostatistics, computational analysis): M. Endo, M. Nakano, T. Kadomatsu, S. Fukuhara, H. Kuroda, T. Hato, H. Horiguchi, M. Harada, H. Horio, Y. Oike

Writing, review, and/or revision of the manuscript: M. Endo, M. Nakano, T. Kadomatsu, H. Iwase, Y. Oike

Administrative, technical, or material support (i.e., reporting or organizing data, constructing databases): M. Endo, M. Nakano, T. Kadomatsu, H. Kuroda, T. Hato, H. Odagiri, T. Masuda, Y. Yamamoto, T. Minami, T. Takahashi, H. Iwase, Y. Oike

Study supervision: M. Endo, T. Kadomatsu, H. Odagiri, H. Nomori, S. Okada, Y. Oike

Acknowledgments

The authors thank S. Iwaki, O. Takahashi, and M. Nakata for technical assistance.

Grant Support

This research is funded by the Japan Society for the Promotion of Science (JSPS) through the "Funding Program for World-Leading Innovative R&D on Science and Technology (FIRST Program)" (LS098), initiated by the Council for Science and Technology Policy (CSTP). This work is also supported by Grants-in-Aid for Scientific Research on Priority Areas from the Ministry of Education, Culture, Sports, Science and Technology of Japan and by grants from the Takeda Science Foundation, the Mitsubishi Foundation, and Tokyo Biochemical Research Foundation.

The costs of publication of this article were defrayed in part by the payment of page charges. This article must therefore be hereby marked *advertisement* in accordance with 18 U.S.C. Section 1734 solely to indicate this fact.

Received December 1, 2011; revised February 10, 2012; accepted February 10, 2012; published OnlineFirst February 16, 2012.

Published OnlineFirst February 16, 2012; DOI:10.1158/0008-5472.CAN-11-3878

References

1. Boyle P, Levin B. World Cancer Report 2008. Lyon, France: IARC Press; 2008.
2. Chiang AC, Massague J. Molecular basis of metastasis. N Engl J Med 2008;359:2814–23.
3. Christofori G. New signals from the invasive front. Nature 2006;441: 444–50.
4. Grivennikov SI, Greten FR, Karin M. Immunity, inflammation, and cancer. Cell 2010;140:883–99.
5. Aoi J, Endo M, Kadomatsu T, Miyata K, Nakano M, Horiguchi H, et al. Angiopoietin-like protein 2 is an important facilitator of inflammatory carcinogenesis and metastasis. Cancer Res 2011;71:7502–12.
6. Mancini M, Toker A. NFAT proteins: emerging roles in cancer progression. Nat Rev Cancer 2009;9:810–20.
7. Muller MR, Rao A. NFAT, immunity and cancer: a transcription factor comes of age. Nat Rev Immunol 2010;10:645–56.
8. Flockhart RJ, Armstrong JL, Reynolds NJ, Lovat PE. NFAT signalling is a novel target of oncogenic BRAF in metastatic melanoma. Br J Cancer 2009;101:1448–55.
9. Koenig A, Linhart T, Schlengemann K, Reutlinger K, Wegele J, Adler G, et al. NFAT-induced histone acetylation relay switch promotes c-Myc-dependent growth in pancreatic cancer cells. Gastroenterology 2010;138:1189–99 e1–2.
10. Yoeli-Lerner M, Yiu GK, Rabinovitz I, Erhardt P, Jauliac S, Toker A. Akt blocks breast cancer cell motility and invasion through the transcription factor NFAT. Mol Cell 2005;20:539–50.
11. Zhang H, Xie X, Zhu X, Zhu J, Hao C, Lu Q, et al. Stimulatory cross-talk between NFAT3 and estrogen receptor in breast cancer cells. J Biol Chem 2005;280:43188–97.
12. Okada T, Tsukano H, Endo M, Tabata M, Miyata K, Kadomatsu T, et al. Synoviocyte-derived angiopoietin-like protein 2 contributes to synovial chronic inflammation in rheumatoid arthritis. Am J Pathol 2010; 176:2309–19.
13. Tabata M, Kadomatsu T, Fukuhara S, Miyata K, Ito Y, Endo M, et al. Angiopoietin-like protein 2 promotes chronic adipose tissue inflammation and obesity-related systemic insulin resistance. Cell Metab 2009;10:178–88.
14. Fukuhara S, Sako K, Minami T, Noda K, Kim HZ, Kodama T, et al. Differential function of Tie2 at cell-cell contacts and cell-substratum contacts regulated by angiopoietin-1. Nat Cell Biol 2008;10:513–26.
15. Kozaki K, Miyaishi O, Tsukamoto T, Tatematsu Y, Hida T, Takahashi T, et al. Establishment and characterization of a human lung cancer cell line NCI-H460-LNM35 with consistent lymphogenous metastasis via both subcutaneous and orthotopic propagation. Cancer Res 2000; 60:2535–40.
16. Jauliac S, Lopez-Rodriguez C, Shaw LM, Brown LF, Rao A, Toker A. The role of NFAT transcription factors in integrin-mediated carcinoma invasion. Nat Cell Biol 2002;4:540–4.
17. Yiu GK, Toker A. NFAT induces breast cancer cell invasion by promoting the induction of cyclooxygenase-2. J Biol Chem 2006;281: 12210–7.
18. Chinenov Y, Kerppola TK. Close encounters of many kinds: Fos-Jun interactions that mediate transcription regulatory specificity. Oncogene 2001;20:2438–52.
19. van Dam H, Castellazzi M. Distinct roles of Jun : Fos and Jun : ATF dimers in oncogenesis. Oncogene 2001;20:2453–64.
20. Chen L, Glover JN, Hogan PG, Rao A, Harrison SC. Structure of the DNA-binding domains from NFAT, Fos and Jun bound specifically to DNA. Nature 1998;392:42–8.
21. Macian F, Lopez-Rodriguez C, Rao A. Partners in transcription: NFAT and AP-1. Oncogene 2001;20:2476–89.
22. Ramirez-Carrozzi V, Kerppola T. Asymmetric recognition of nonconsensus AP-1 sites by Fos-Jun and Jun-Jun influences transcriptional cooperativity with NFAT1. Mol Cell Biol 2003;23:1737–49.
23. Szabo E, Riffe ME, Steinberg SM, Birrer MJ, Linnoila RI. Altered cJUN expression: an early event in human lung carcinogenesis. Cancer Res 1996;56:305–15.
24. Shimizu Y, Kinoshita I, Kikuchi J, Yamazaki K, Nishimura M, Birrer MJ, et al. Growth inhibition of non-small cell lung cancer cells by AP-1 blockade using a cJun dominant-negative mutant. Br J Cancer 2008; 98:915–22.
25. Okada S, Harada H, Ito T, Saito T, Suzu S. Early development of human hematopoietic and acquired immune systems in new born NOD/Scid/Jak3null mice intrahepatic engrafted with cord blood-derived CD34 + cells. Int J Hematol 2008;88:476–82.
26. Waterman-Storer CM, Worthylake RA, Liu BP, Burridge K, Salmon ED. Microtubule growth activates Rac1 to promote lamellipodial protrusion in fibroblasts. Nat Cell Biol 1999;1:45–50.
27. Kao J, Salari K, Bocanegra M, Choi YL, Girard L, Gandhi J, et al. Molecular profiling of breast cancer cell lines defines relevant tumor models and provides a resource for cancer gene discovery. PLoS One 2009;4:e6146.
28. Lopez-Bergami P, Lau E, Ronai Z. Emerging roles of ATF2 and the dynamic AP1 network in cancer. Nat Rev Cancer 2010;10: 65–76.
29. Vlahopoulos SA, Logotheti S, Mikas D, Giarika A, Gorgoulis V, Zoumpourlis V. The role of ATF-2 in oncogenesis. Bioessays 2008;30: 314–27.
30. Moenner M, Pluquet O, Bouchecareilh M, Chevet E. Integrated endoplasmic reticulum stress responses in cancer. Cancer Res 2007;67: 10631–4.
31. Xu C, Bailly-Maitre B, Reed JC. Endoplasmic reticulum stress: cell life and death decisions. J Clin Invest 2005;115:2656–64.
32. Crabtree GR, Olson EN. NFAT signaling: choreographing the social lives of cells. Cell 2002;109 Suppl: S67–79.
33. Crawford Y, Kasman I, Yu L, Zhong C, Wu X, Modrusan Z, et al. PDGF-C mediates the angiogenic and tumorigenic properties of fibroblasts associated with tumors refractory to anti-VEGF treatment. Cancer Cell 2009;15:21–34.
34. Minami T, Horiuchi K, Miura M, Abid MR, Takabe W, Noguchi N, et al. Vascular endothelial growth factor- and thrombin-induced termination factor, Down syndrome critical region-1, attenuates endothelial cell proliferation and angiogenesis. J Biol Chem 2004; 279:50537–54.
35. Minami T, Yano K, Miura M, Kobayashi M, Suehiro J, Reid PC, et al. The Down syndrome critical region gene 1 short variant promoters direct vascular bed-specific gene expression during inflammation in mice. J Clin Invest 2009;119:2257–70.
36. Sanz-Moreno V, Gadea G, Ahn J, Paterson H, Marra P, Pinner S, et al. Rac activation and inactivation control plasticity of tumor cell movement. Cell 2008;135:510–23.

OPEN ACCESS Freely available online

PLOS ONE

Fenton Reaction Induced Cancer in Wild Type Rats Recapitulates Genomic Alterations Observed in Human Cancer

Shinya Akatsuka[1], Yoriko Yamashita[1], Hiroki Ohara[1], Yu-Ting Liu[2], Masashi Izumiya[3], Koichiro Abe[3,4], Masako Ochiai[3], Li Jiang[1], Hirotaka Nagai[1,2], Yasumasa Okazaki[1], Hideki Murakami[5], Yoshitaka Sekido[5], Eri Arai[6], Yae Kanai[6], Okio Hino[7], Takashi Takahashi[8], Hitoshi Nakagama[3], Shinya Toyokuni[1]*

1 Departments of Pathology and Biological Responses, Nagoya University Graduate School of Medicine, Showa-ku, Nagoya, Japan, **2** Department of Pathology and Biology of Diseases, Kyoto University Graduate School of Medicine, Sakyo-ku, Kyoto, Japan, **3** Division of Cancer Development System, National Cancer Center Research Institute, Chuo-ku, Tokyo, Japan, **4** Department of Internal Medicine, Teikyo University School of Medicine, Itabashi-ku, Tokyo, Japan, **5** Division of Molecular Oncology, Aichi Cancer Center Research Institute, Chikusa-Ku, Nagoya, Japan, **6** Division of Molecular Pathology, National Cancer Center Research Institute, Chuo-ku, Tokyo, Japan, **7** Department of Pathology and Oncology, Juntendo University School of Medicine, Bunkyo-ku, Tokyo, Japan, **8** Molecular Carcinogenesis, Nagoya University Graduate School of Medicine, Showa-ku, Nagoya, Japan

Abstract

Iron overload has been associated with carcinogenesis in humans. Intraperitoneal administration of ferric nitrilotriacetate initiates a Fenton reaction in renal proximal tubules of rodents that ultimately leads to a high incidence of renal cell carcinoma (RCC) after repeated treatments. We performed high-resolution microarray comparative genomic hybridization to identify characteristics in the genomic profiles of this oxidative stress-induced rat RCCs. The results revealed extensive large-scale genomic alterations with a preference for deletions. Deletions and amplifications were numerous and sometimes fragmented, demonstrating that a Fenton reaction is a cause of such genomic alterations *in vivo*. Frequency plotting indicated that two of the most commonly altered loci corresponded to a *Cdkn2a/2b* deletion and a *Met* amplification. Tumor sizes were proportionally associated with *Met* expression and/or amplification, and clustering analysis confirmed our results. Furthermore, we developed a procedure to compare whole genomic patterns of the copy number alterations among different species based on chromosomal syntenic relationship. Patterns of the rat RCCs showed the strongest similarity to the human RCCs among five types of human cancers, followed by human malignant mesothelioma, an iron overload-associated cancer. Therefore, an iron-dependent Fenton chemical reaction causes large-scale genomic alterations during carcinogenesis, which may result in distinct genomic profiles. Based on the characteristics of extensive genome alterations in human cancer, our results suggest that this chemical reaction may play a major role during human carcinogenesis.

Citation: Akatsuka S, Yamashita Y, Ohara H, Liu Y-T, Izumiya M, et al. (2012) Fenton Reaction Induced Cancer in Wild Type Rats Recapitulates Genomic Alterations Observed in Human Cancer. PLoS ONE 7(8): e43403. doi:10.1371/journal.pone.0043403

Editor: Kamaleshwar Singh, Texas Tech University, United States of America

Received March 2, 2012; **Accepted** July 19, 2012; **Published** August 29, 2012

Funding: This study was supported by Princess Takamatsu Cancer Research Fund (10-24213); a Grant-in-Aid for Cancer Research from the Ministry of Health, Labour and Welfare of Japan; and a Grant-in Aid from the Ministry of Education, Culture, Sports, Science and Technology of Japan. The funders had no role in study design, data collection and analysis, decision to publish, or preparation of the manuscript.

Competing Interests: The authors have declared that no competing interests exist.

* E-mail: toyokuni@med.nagoya-u.ac.jp

Introduction

Cancer is a disease of accumulated genomic alterations, presumably caused by a systematic process during cellular injury and repair. Causative agents for carcinogenesis are numerous including γ-radiation, ultraviolet radiation, inflammation, chemicals and iron overload [1]. Genomic data of a variety of human cancers is currently analyzed either with array-based comparative genomic hybridization (CGH) [2] or next-generation sequencing [3,4]. These projects are performed to find causative gene mutations that will lead to identifying novel chemicals or antibodies directed for the interactions of responsible signaling molecules. These efforts are expected to result in developments of effective drugs. However, cancer prevention in daily life is as important as its therapy.

In the present study, we sought to resolve roles of iron-mediated oxidative stress during carcinogenesis using array-based CGH. Oxidative stress is constitutively caused by the metabolism of molecular oxygen [5], but is mainly regulated by various antioxidant systems. However, in a variety of pathological conditions, oxidative stress loads exceed the antioxidant capacity [6]. Iron is the most abundant heavy metal in mammals, such as rodents and humans. Whereas iron is essential for oxygen transport as a component of hemoglobin, excess iron has been associated with carcinogenesis [7,8], presumably through a Fenton reaction [9]. Ionic forms of iron are barely soluble at a neutral pH, but ferric nitrilotriacetate (Fe-NTA), an iron chelate, is soluble at pH 7.4 and is an efficient catalytic agent for the Fenton reaction [10]. In the 1980s, our group established that repeated intraperitoneal administrations of Fe-NTA induce a high incidence of renal cell carcinoma (RCC) in rodents [11,12]. Later, we

showed that the renal injury occurs through a Fenton reaction with a variety of hydroxyl radical-mediated chemical products, such as 8-hydroxy-2′-deoxyguanosine [13,14] and 4-hydroxy-nonenal [15,16]. It is established that an iron overload in many pathological conditions is associated with the presence of catalytic iron [17,18].

Accordingly, by evaluating whole genome of RCCs, we could find a general principle for the genomic alterations under oxidatively-stressed conditions. We reported a *Cdkn2a/2b* deletion using microsatellite analysis in this model [19]. In this study, we evaluated the whole genome of Fe-NTA-induced rat RCCs and their cell lines using array-based CGHs. Furthermore, we transformed the data into a human genome through chromosomal syntenic relationship and analyzed the association.

Results

Genome-wide Views of DNA Copy Number Alterations in Fe-NTA-induced Rat RCCs

Fifteen rat RCC DNA samples, which included 13 primary tumor samples and 2 cell line samples, were hybridized on Agilent oligonucleotide microarrays for CGH with 181,978 genomic loci (GEO accession: GSE36101). Comparing different array-based CGH profiles in a quantitative manner is difficult. A shift in the mean copy number is caused by polyploidy and the contamination of normal cells. Therefore, we have developed a statistical method that considers these factors to estimate the chromosomal copy number (**Methods S1**). In this paper, array-based CGH profile data analyses are based on the estimated copy numbers using this method.

Array-based CGH profiling revealed that genomes of the Fe-NTA-induced rat RCCs are often complex and have many extensive chromosomal alterations (**Figs. 1A and S1**). A whole genome frequency analysis with 15 samples identified recurrent regions of a copy number aberration in the Fe-NTA-induced RCCs (**Fig. 1B**). Copy number aberrations were determined based on the distribution of the log2 ratio values that were recalculated with the estimated copy number for a set of 13 primary tumors and 2 cell lines (**Fig. S2**). In this distribution, the thresholds that represented gain and loss were chosen at ± 0.377. A threshold representing amplification was chosen at +0.811 whereas a homozygous deletion (complete loss) was assigned to the position at which the copy number was estimated as 0. The most characteristic global feature uncovered by the frequency analysis was a predisposition to lose an extensively wide region of chromosomes, especially for chromosomes 3, 5, 6, 8, 9, 14, 15, 17 and 20. The second feature was a frequent amplification over a long pericentromeric region in chromosome 4.

Frequent Chromosomal Loss in Rat Chromosome 5 and Homozygous Deletion at the *Cdkn2a/2b* Locus

Chromosome 5 underwent an extensive loss in copy number, not less than that in other chromosomes (e.g., chromosomes 6, 8 and 20) (**Fig. 1B**). As it relates to extensive loss, homozygous deletions were most frequently observed at the *Cdkn2a/2b* locus on chromosome 5 (**Fig. 2A**). This commonly deleted region included two loci (*Cdkn2a* and *Cdkn2b*) for three distinct tumor suppressor genes (*p16* and *p19* in *Cdkn2a*; *p15* in *Cdkn2b*) (**Fig. 2B**). Shutdown of *p16/p19* and *p15* mRNA expression was confirmed in the samples that contained a homozygous deletion at the *Cdkn2a/2b* locus (**Figs. 2C and 2D**). In samples with a hemizygous deletion at the *Cdkn2a* locus (i.e., FB32-4, FB28-7), *p16* and *p19* expressions were downregulated, presumably because the promoter regions of the remaining alleles were methylated. However, some of the samples with either a hemizygous or no deletion (e.g., FB14-3; BF51-1; FB14-6; FB30-5 and FB33-7) showed a marked over-expression of *p16* and *p19*.

Frequent Amplifications Over the Pericentromeric Region of Chromosome 4 and Amplification at the *Met* Locus

Over a long portion of the pericentromeric region in chromosome 4, frequent copy number gain and amplification were observed (**Fig. 1B**). Genomic amplification and gene expression in the corresponding areas of chromosome 4 were mostly proportional (**Fig. S3**). A bar plot of the amplified region along the pericentromeric region in chromosome 4 revealed that *Met* oncogene resides in the most common overlapping genomic section (**Fig. 3A**). The most overlapping section with a length of approximately 222 kb consisted of an amplified region in 11/15 samples and contained only one RefSeq-curated gene (*Met*) (**Fig. 3B**). A greater than 5-fold increase in *Met* mRNA expression was observed in 6 samples among the 9 tumors that contained a genomic amplification of *Met* (**Fig. 3C**).

Collectively, regarding chromosomal aberrations at these two cancer-related loci, every examined carcinoma including the two cell lines contained either the *Met* amplification or the *Cdkn2a/2b* deletion (**Table 1, Figs. 2B and 3B**). Other common genetic alterations are summarized in **Table S1** (20 deleted genes, common in 2–4 RCC tumors) and **Table S2** (340 amplified genes, common in 2–9 RCC tumors). Among those *Zbtb38* amplification was confirmed for overexpression (**Fig. S4**).

Tumor Size of Fe-NTA-induced RCCs is Regulated by Genetic Features

We examined the associations between genetic alterations and various RCC traits including those summarized in **Table 1**. Among all of the relationships examined, *Met* expression and tumor size were proportionally associated (**Fig. 4A**). Furthermore, a hierarchical clustering of tumors based on whole patterns of chromosomal changes revealed that a group of large tumors (i.e., FB7-7, FB30-5 and FB33-7) corresponded to a distinct cluster (**Fig. 4B**). Therefore, a tumor trait, size at the time the tumor was clinically overt, was associated with the entire array-based CGH profiles.

Comparison of Copy Number Alteration Profiles in Cancer Genomes Between Rats and Humans

To determine the general principle of large-scale genomic changes in cancer across mammalian species, we compared cancer genomes of rats and humans as a whole spectrum of chromosomal alterations. First, we transformed the rat array-based CGH profiles onto human chromosomes according to a synteny between the two species. Thereafter, we compared the whole patterns based on estimated copy numbers using multidimensional data analysis methods. We found that Fe-NTA-induced rat RCC was most similar to human RCCs, followed by human malignant mesothelioma (**Figs. 5A and 5B**).

Discussion

In this study, we report for the first time analyses of the entire data from array-based CGH applied to a Fenton chemistry-induced carcinogenesis in a rat kidney model [20]. We found that oxidative stress causes extensive genomic alterations in the induced cancer genome at chromosomal level (**Fig. 1A**). It is well known that a majority of human malignant solid tumors possess gains or losses in numerous chromosomes [21,22], and amplification can

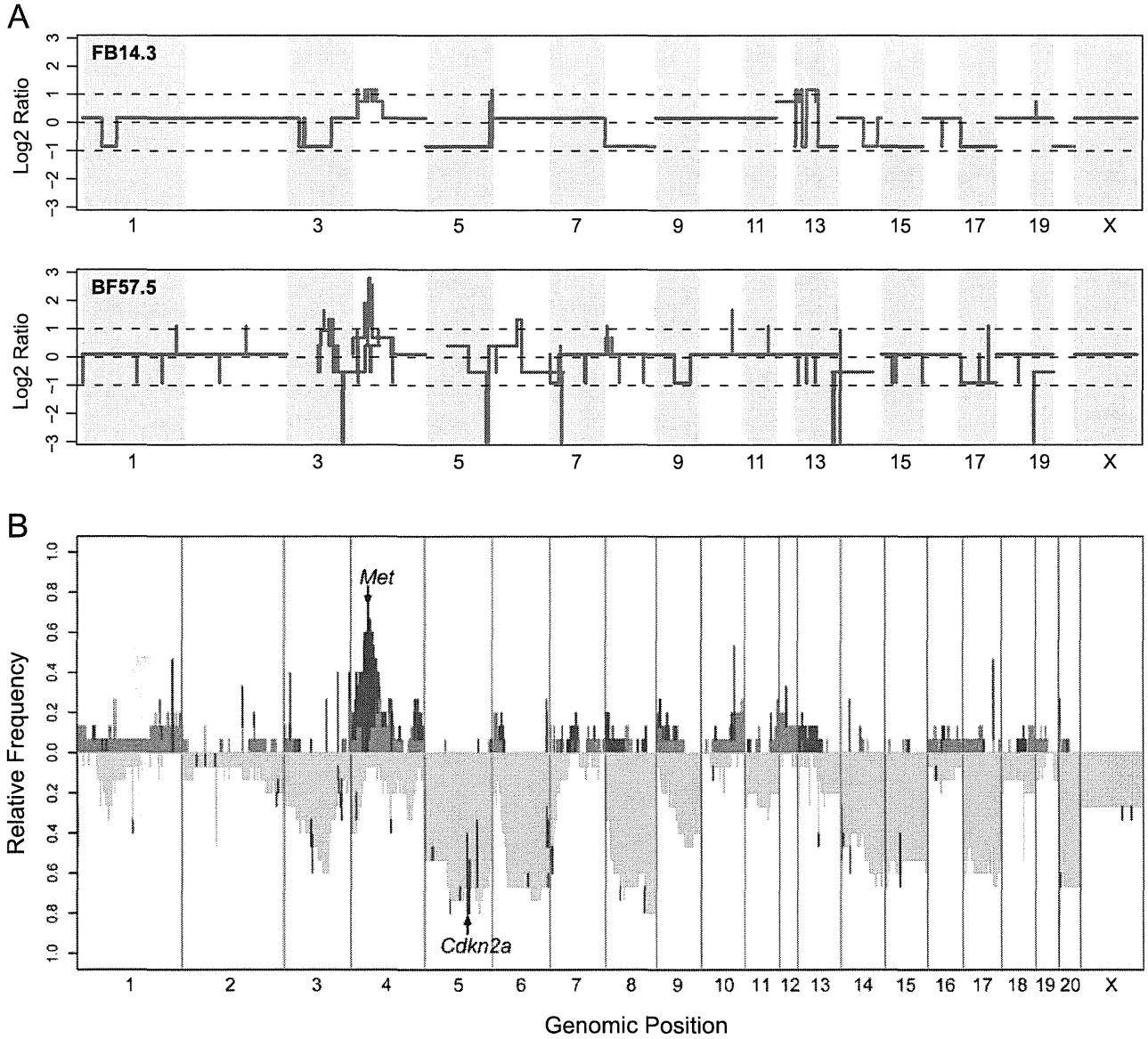

Figure 1. Genome-wide views of DNA copy number alterations in Fe-NTA induced rat renal cell carcinomas (RCCs). (A) Representative array-based CGH profiles from two RCC tumors. The red lines show log2 ratios of the estimated copy number over the inferred cancer ploidy versus the genomic position for all of the CGH microarray probes. (B) Frequency distribution of copy number aberrations across the whole rat genome. The relative frequencies of amplification (dark red), gain (tomato), loss (green yellow) and homozygous deletion (dark green) within 13 RCC tumors and two RCC cell lines are plotted at each genomic position. Two cancer-related loci, *Met* and *Cdkn2a*, which were most frequently affected by copy number aberration are indicated by the arrows.
doi:10.1371/journal.pone.0043403.g001

be a suitable target for cancer chemotherapy. During the carcinogenic process of such tumors, chromosomal instability is thought to contribute as a driving factor [23]. Among wild-type rodent carcinogenesis models, however, few models report using primary tumor samples extensive genetic alterations because of chromosomal instability [24,25]. Radiation-induced murine malignant lymphoma [26] and murine lung adenocarcinoma induced by 4-(methylnitrosamino)-1-(3-pyridyl)-1-butanone, a carcinogen present in tobacco smoke [27], revealed slightly more gross chromosomal aberrations than the corresponding spontaneous tumors, albeit the low resolution in the report (bacterial artificial chromosome [BAC] array of ~6,500). The facts that control rats exhibit no RCCs [11,12] and Fe-NTA-induced rat RCC model exhibits an equivalence to human cancers in genomic alterations at chromosomal level strongly support the idea that this carcinogenesis model mimics an actual carcinogenic process in those humans who lack strong cancer susceptibility traits.

Conversely, mice with multiple genetically-engineered cancer-associated genes show genetic alteration of this kind [28]. We think that those experiments correspond to an established mutator phenotype [29] and, thus, to the carcinogenic process in humans who have strong cancer susceptibility traits such as Li-Fraumeni syndrome (*p53*) [30] or melanoma kindreds (*p16*) [31]. As a hereditary rat RCC model, we also analyzed the RCCs of Eker rats, which do not show aggressive characteristics, such as metastasis [32,33,34]. We observed that these RCCs showed null

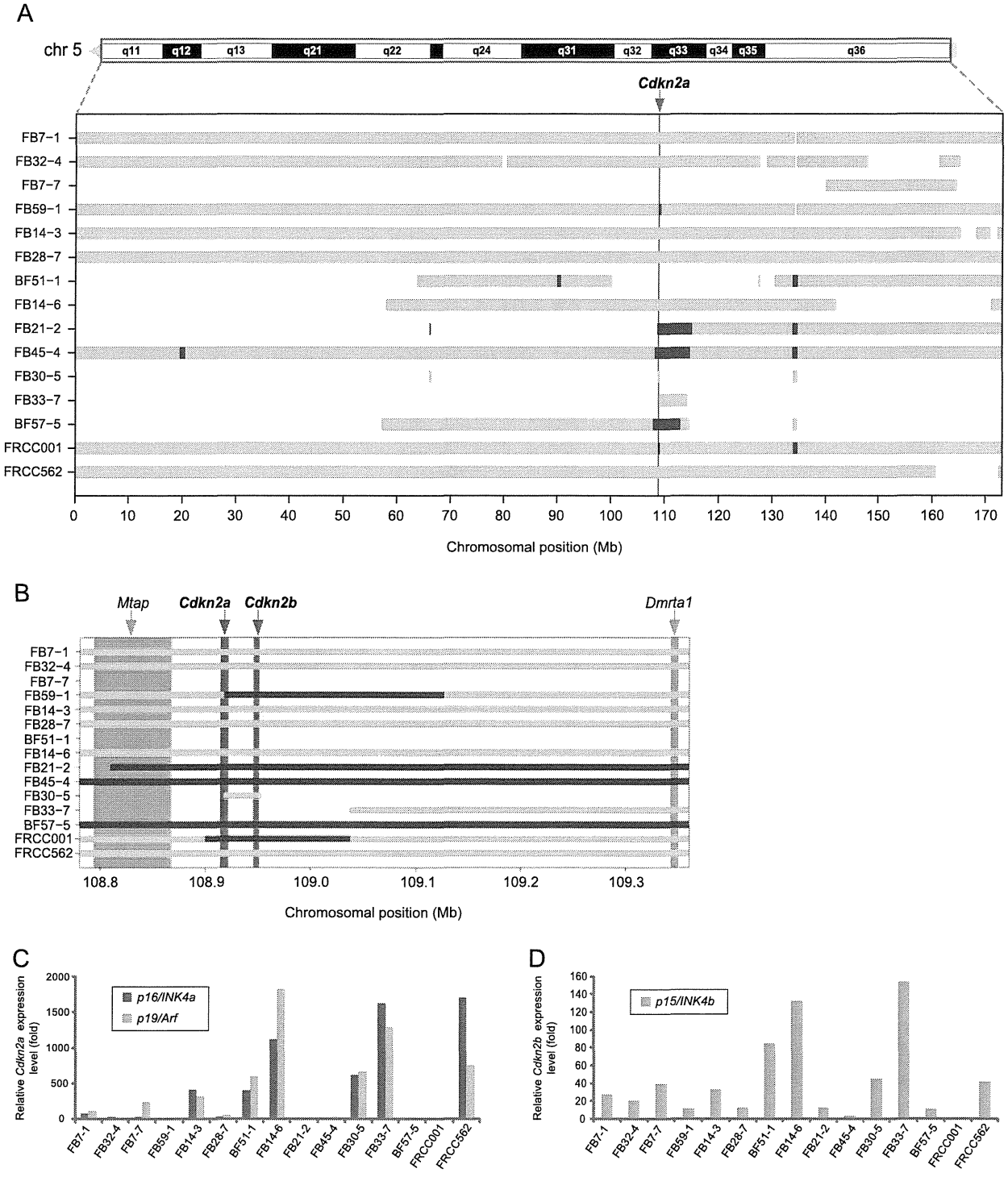

Figure 2. Frequent extensive chromosomal losses in rat chromosome 5, and homozygous deletions at the region including the *Cdkn2a* and *Cdkn2b* loci. (A) The bar chart represents the regions of chromosomal loss (green yellow) and homozygous deletion (dark green) along chromosome 5 for 13 RCC tumors and two RCC cell lines. The vertical red line on the background indicates the position of the *Cdkn2a* locus. (B) Magnified view of the bar chart centered on the *Cdkn2a/2b* loci. The genomic regions of all of the RefSeq genes included in the displayed range of the chromosome are depicted as vertical bars on the background. (C) Expression analysis of *Cdkn2a* ($p16^{Ink4a}$ and $p19^{Arf}$) for 13 RCC tumors and two RCC cell lines, using real-time PCR with specific primer pairs for each different transcript. The values on the *y*-axis indicate relative mRNA expression level compared to an average of those in normal kidneys of three control rats. (D) Expression analysis of *Cdkn2b* ($p15^{Ink4b}$) for 13 RCC tumors and two RCC cell lines by real-time PCR. The values on the *y*-axis indicate relative mRNA expression level compared to an average of those in normal kidneys of three control rats.

doi:10.1371/journal.pone.0043403.g002

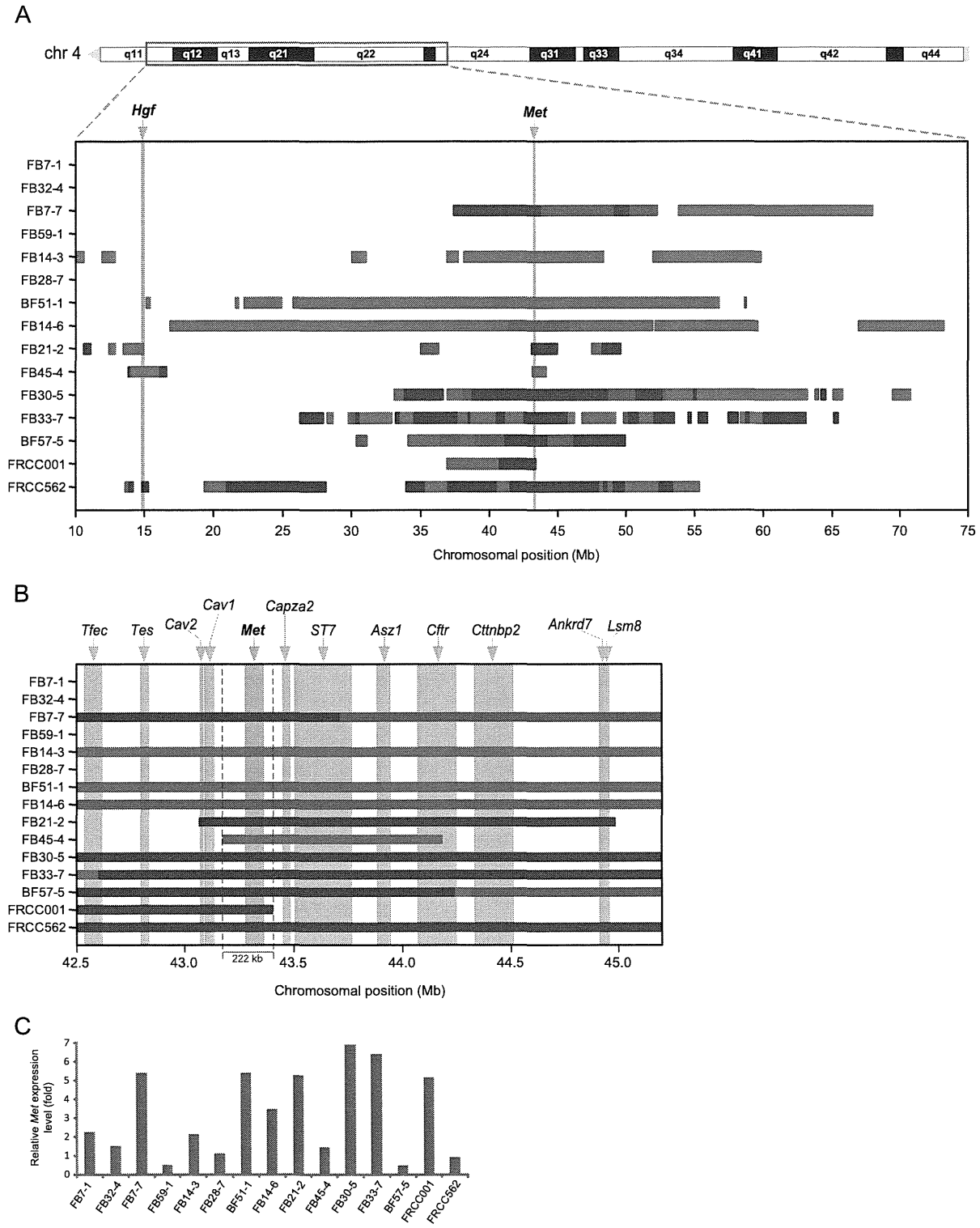

Figure 3. Frequent wide-ranging amplifications over a long pericentromeric region of chromosome 4 with the *Met* oncogene residing in the most overlapping section. (A) The bar chart represents the amplification regions along a 65 Mb pericentrometic region of chromosome 4 for 13 RCC tumors and two RCC cell lines. Four grades of amplification are indicated by bar color gradation; the darker the red, the larger the amplitude. (B) A magnified view of the bar chart above shows the vicinity of the most overlapping region. The genomic regions of all of the RefSeq genes included in the displayed range of the chromosome are depicted as vertical bars in the background. (C) Expression analysis of *Met* for 13 RCC tumors and two RCC cell lines by real-time PCR. The values on the *y*-axis indicate relative mRNA expression level compared to an average of those in normal kidneys of three control rats.
doi:10.1371/journal.pone.0043403.g003

Table 1. Features of 13 cases of Fe-NTA-induced renal cell carcinomas.

						Copy number aberration at	
Tumor case	**Size (mm)**	**Metastasis**	**Invasion**	**Nuclear atypia grade**	**Growth pattern**	***Met* locus**	***Cdkn2a/2b* locus**
FB7-1	20	None	None	Low	Intermediate	None	Loss
FB32-4	15	Lung	None	Intermediate	Intermediate	None	Loss
FB7-7	60	Lung	None	Intermediate	Expansive	Amplification	None
FB59-1	15	Lung	Peritoneal	Intermediate	Infiltrating	None	HD
FB14-3	15	None	None	High	Expansive	Amplification	Loss
FB28-7	30	None	None	High	Intermediate	None	Loss
BF51-1	28	None	None	High	Intermediate	Amplification	None
FB14-6	30	Lung	Peritoneal	High	Intermediate	Amplification	Loss
FB21-2	40	None	None	High	Infiltrating	Amplification	HD
FB45-4	40	Lung	None	High	Infiltrating	Amplification	HD
FB30-5	60	Lung	Peritoneal	High	Infiltrating	Amplification	Loss
FB33-7	70	Lung	Peritoneal	High	Infiltrating	Amplification	None
BF57-5	25	Lung	Peritoneal	High	Infiltrating	Amplification	HD

Fe-NTA: ferric nitrilotriacetate; HD: homozygous deletion.
doi:10.1371/journal.pone.0043403.t001

or subtle genetic alterations (**Fig. S5**). Accordingly, oxidative stress, including that induced due to excess iron, could be one of the causes of human renal carcinogenesis. Indeed, numerous epidemiological studies have associated iron and steel industry workers with an increased RCC risk [35].

A frequency plot analysis revealed two remarkable features. First, the chromosomal aberrations showed a preference for loss against the ploidy of each cancer genome. Mostly, the aberration was represented by a deletion at either a whole chromosomal level (monosomy) or at a segmental level (**Fig. 1B**). The most common target for loss was the *Cdkn2a/2b* locus. The predominance of loss in the profile of chromosomal alterations may be attributed to the early stage of carcinogenesis. We previously demonstrated that cells with a hemizygous deletion at *Cdkn2a* appear as early as a few weeks after initiating a Fe-NTA administration [36].

Our present analysis revealed that the monoallelic loss of chromosome 5 in its entirety or of an equivalently wide region is the major first event. Indeed, we found only one case (6.7%) of a monoallelic loss of an extremely narrow region (~350 kilobases; **Figs. 2A and 2B**). Fe-NTA catalyzes the generation of hydroxyl radicals through a Fenton reaction specifically in the lumina of renal proximal tubules, which leads to degeneration and necrosis/apoptosis of those cells [37,38]. Because kidney is a vital organ that performs urea excretion, reabsorption of valuable molecules as

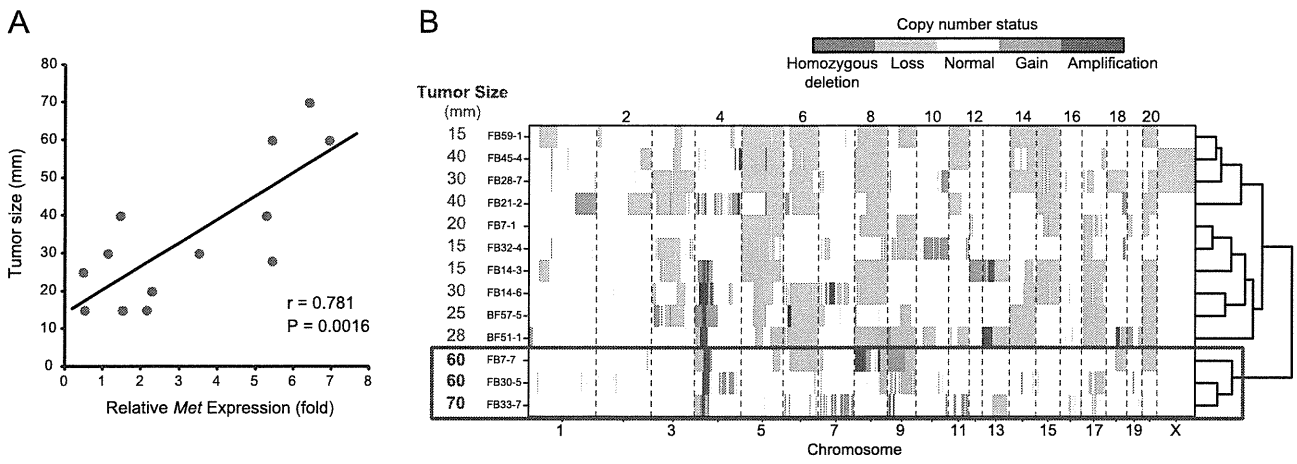

Figure 4. Tumor sizes of Fe-NTA induced RCCs are controlled by the genetic features. (A) *Met* expression is significantly correlated with tumor size. Pearson's correlation coefficient (r) and the corresponding P value are written on the plot area. (B) Hierarchical clustering of the RCC tumors based on the whole genome patterns of the copy number changes. The large-size tumors form a distinct cluster.
doi:10.1371/journal.pone.0043403.g004

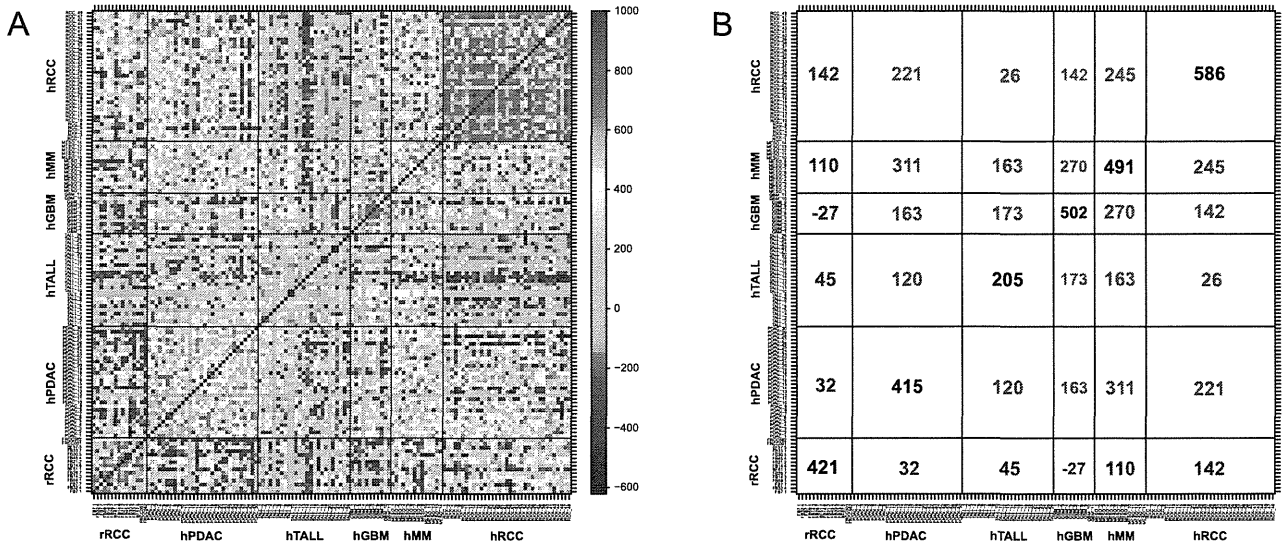

Figure 5. Comparison of copy number alteration profiles in cancer genomes between Fe-NTA-induced rat RCCs and human tumors. (A) The color plot represents a similarity matrix across the rat RCCs and various human cancers. rRCC, rat renal cell carcinoma; hPDAC, human pancreatic ductal adenocarcinoma; hTALL, human T-cell acute lymphoblastic leukemia; hGBM, human glioblastoma multiforme; hRCC, human renal cell carcinoma. (B) Numerical summary of the similarity matrix. The number in each square indicates an average value of similarity index (defined between −1000 and 1,000). Refer to the Materials and Methods section for details.
doi:10.1371/journal.pone.0043403.g005

well as ionic homeostasis maintenance, regeneration from the remaining tubular cells is intensely promoted. Under chronic oxidative stress by repeated Fe-NTA administrations, this degeneration and regeneration process would continue for months to years, increasing the risk of mitotic events simultaneously with the repair of oxidative DNA damage. We believe that this oxidative stress causes abnormal DNA replication and chromosomal missegregation, which leads to the emergence of aneuploid cells. Surprisingly, this series of events appear to occur in months, leading to a high incidence (~90%) of RCC in rats within two years. Aneuploid cells usually exhibit phenotypes consistent with increased energy need and proteotoxic stress. However, aneuploidy can promote tumorigenesis under the following two hypothetical mechanisms: 1) aneuploidy may cause a proliferative advantage through loss of G1/S transition control under conditions in which normal euploid cells do not divide [39] and 2) aneuploidy can advance tumorigenesis by promoting genomic instability, hence increasing the evolvability of tumors [40]. The frequent deletion of the *Cdkn2a/2b* locus is observed in the rat peritoneal mesothelioma, an iron overload-associated tumor [41], induced either by another iron compound (ferric saccharate) [42] or by asbestos [43]. These common traits of animal models strongly suggest that *Cdkn2a/2b* is a principal target in iron-mediated carcinogenesis. The same genetic alteration is observed in rat mesothelioma induced by multi-walled carbon nanotubes [44], in which iron involvement is not yet established. We would like to add here for the biological significance of our results that homozygous deletion of *CDKN2A/2B* is frequently observed in human mesothelioma associated with asbestos exposure [**45,46**].

Some of the tumors with a remaining *Cdkn2a/2b* allele showed extremely high expression levels of two products from this locus, *p16/Ink4a* and *p19/Arf*. This is a currently debated issue in human cancer [47]. There is considerable evidence that several neoplasms exhibit significant p16 levels in cytoplasm [48]. This can be an unsuccessful attempt to stop cell proliferation in the case of downstream *Rb* dysregulation [49] or may represent an alternative mechanism for modulating unidentified pathways. Our data exhibit ~50% hemizygous deletion of *Rb*. This requires further clarification with epigenetic analysis.

The second feature determined using frequency plot analysis was a high incidence of amplification along a limited chromosomal region toward the centromere of chromosome 4, pointing to the *Met* locus. A region spanning 80 Mb from the centromere of rat chromosome 4 is syntenic to human chromosome 7. Various human cancers, such as glioblastoma [50] and non-small cell lung cancer [51], are reported to harbor amplifications in chromosome 7. Tyrosine kinase MET is a receptor for a hepatocyte growth factor and is situated upstream of *ras* in the signal transduction pathway, thus serving as an advantage for cell proliferation [52]. Therefore, it is conceivable that tumor size was proportionally associated with the *Met* expression level (**Figs. 3C and 4A**). Because we dissect the animal as soon as we recognize the tumor, we believe that large-sized tumors are more aggressive in nature. It is of note that tumor size was also related to the genome alteration pattern (**Fig. 4B**), and was associated with amplification and overexpression of *Zbtb38* located on chromosome 8 (**Fig. S4**). ZBTB38 (CIBZ) represses the transcription of methylated templates [53], thus presumably regulating epigenetic mechanisms. Down-regulation of ZBTB38, a novel substrate of caspase-3, induces apoptosis [54] and this gene is localized in a prostate cancer susceptibility locus [54]. These results confirm the possibility of tumor classification using array-based CGH. *Met* arose evolutionally late and is unique to mammals [52]; it could thereby be associated with the unique amplification in the whole genome.

Genomic amplification is hypothesized to occur via the breakage-fusion-bridge cycle [55,56,57]. A Fenton reaction causes double-stranded DNA breakage [10]. Our results revealed that these amplifications consisted of a mixture of wide-range low-level amplifications and fragmented, narrow high-level amplifications

(**Fig. 3A**). This suggests a mechanism of positive feedback for amplification, starting from wide-range low-level amplification. We suspect an involvement of double-minutes, and a presence of susceptible genomic loci. This hypothesis requires further study. It was interesting that two tumor suppressive genes, *Cav1* [58,59] and *ST7* [60], surrounded the *Met* locus (**Fig. 3B**). This may be the reason why the *Met* locus was a denominator for the rat RCCs. Whole exome or genome sequencing may further reveal new findings regarding point mutation and chromosomal translocation.

Finally, we compared the present rat results with corresponding human tumors by transforming data based on chromosomal synteny (**Figs. 5A and 5B**). It was expected that the genomic alteration of Fe-NTA-induced rat RCC was most similar to human RCC presumably because target cells are the same. However, surprisingly, human mesothelioma was the second most similar. It is now established that most human mesothelioma results from exposure to asbestos, and the primary pathogenic process involved is iron overload [**8,61**]. The same mesodermal origin of renal tubular cells and mesothelial cells may cause the similarity of the array-based CGH profiles. Endodermal tumor, such as pancreatic ductal adenocarcinoma (PDAC), and ectodermal tumor, such as glioblastoma multiforme (GBM), exhibited a significant difference in genomic profiles.

In conclusion, we showed that repeated Fenton reactions in wild-type rats induced cancer that recapitulated genomic alterations similar to those in human cancers, suggesting the involvement of oxidative stress as a major factor in human carcinogenesis. In this renal carcinogenesis model, preferred alterations were deletion; *Cdkn2A/2B* deletion and *Met* amplification were the major target gene modifications. A comparative interspecies analysis would contribute to identifying candidate carcinogenic agents.

Materials and Methods

Fe-NTA-induced Renal Cell Carcinoma Model

Fe-NTA-induced carcinogenesis experiments were performed using male F1 hybrid rats that were a cross between Fischer 344 and Brown-Norway inbred strains (Charles River, Yokohama, Japan) as previously described [62]. Thirteen RCC cases were used in this study, and the histological grade of the tumor was determined according to the modified World Health Organization classification as we previously described [62]. The details are summarized in **Table 1**. The animal experiment committees of the Graduate School of Medicine, Kyoto University Graduate School of Medicine and Nagoya University Graduate School of Medicine approved this study. FRCC001 and FRCC562 cell lines were established from primary Fe-NTA-induced RCCs as previously described [63].

Array-based Comparative Genomic Hybridization

Genomic DNA from the tumors and the cell lines was isolated with DNeasy (Qiagen, Valencia, CA). Array-based CGH was performed with an Agilent 185 K rat genome CGH microarray (Agilent Technologies, Santa Clara, CA) as previously described [64]. Thirteen primary tumors and two cell lines of Fe-NTA induced RCCs were analyzed using reference DNA extracted from a normal kidney of a rat from Brown-Norway imbred strain. One RCC sample of a female Eker rat [32] was analyzed using reference DNA extracted from a normal kidney of a male Eker rat. Two additional RCC samples of male Eker rats were analyzed with Rat Genome CGH Microarray 105A (G4436A; Agilent Technologies), using reference DNA extracted from a normal liver of another male Eker rat. The normalized array-based CGH data were processed to generate a segmented profile by circular binary segmentation (CBS) [65] with an altered significance level (alpha = 0.0001). The procedure of data processing for copy number estimation is detailed in **Methods S1**.

Quantitative RT-PCR Analysis

Total RNA was isolated using Isogen reagents (Nippon Gene Co. Ltd., Tokyo, Japan) according to the manufacturer's protocol. cDNA was synthesized using an RNA PCR kit ver. 3.0 (Takara Bio, Shiga, Japan) with random primers. A Platinum SYBR Green qPCR SuperMix-UDG kit (Invitrogen, Carlsbad, CA) and a 7300 Real-Time PCR System (Applied Biosystems, Foster City, CA) were used for quantitative real-time PCR analysis. Rat β-actin was used as an internal control. The primers used were as follows: $p16^{Ink4a}$, 5′-aaacgccccgaacactttc-3′ and 5′-gttcgaatctgcaccatagga-3′; $p19^{Arf}$, 5′-accccaagtgagggttttct-3′ and 5′-agagctgccactttgacgtt-3′; $p15^{Ink4b}$, 5′-tccacaggctagagggaaaa-3′ and 5′-gtgcaggt-gactccttggtt-3′; *Met*, 5′-ttaagcgagagcacgacaaat-3′ and 5′-ccacatag-gaaaacgcactgt-3′; *Zbtb38*, 5′-gtagctgctgctccaaatcc-3′ and 5′-cctgttgagggtggtgaact-3′; β-actin, 5′-tgtgttgtccctgtatgcctctg-3′ and 5′-atagatgggcacagtgtgggtg-3′.

Human Data

We used human array-based CGH data of pancreatic ductal adenocarcinoma (hPDAC) [28], T-cell acute lymphoblastic leukemia (hTALL) [28], glioblastoma (hGBM) [66], mesothelioma cell line (hMM) [67] and renal cell carcinoma (hRCC) [56]. The Agilent CGH-array data of the former four types of human cancer were obtained from NCBI's Gene Expression Omnibus (GEO) website (http://www.ncbi.nlm.nih.gov/geo/). The GEO accession numbers for the data sets are GSE7599 (hPDAC), GSE7603 (hTALL), GSE9177 (hGBM) and GSE22237 (hMM). The human RCC data was obtained through analyses with BAC microarrays (4,361 clones) [68]. We defined similarity index between the two array-based CGH profiles as follows. First, we calculated the correlation coefficient with log2 ratios of the estimated copy number over the inferred cancer ploidy for the genomic positions corresponding to all of the Agilent 44 K human CGH microarray probes. Then, we multiplied the value by 1×10^3 after changing the absolute value into its square root.

Supporting Information

Figure S1 Array-CGH profiles from all the RCCs examined. Red lines show log2 ratios of estimated copy number over inferred cancer ploidy versus genomic position for all the CGH microarray probes.
(PDF)

Figure S2 Distribution of log2 ratio values of estimated copy number for all the probes in all the microarrays performed.
(PDF)

Figure S3 Example of global expression changes in line with genomic alteration. Differences in genome and transcriptome are analyzed between two RCCs, FB7-7 having wide-range amplification on chromosome 4 versus FB28-7 having no substantial genomic alteration on chromosome 4. (A) Sky blue circle plot indicates ratio of estimated copy numbers based on array-based CGH (FB7-7 *vs* FB28-7). Red circle plot indicates ratio of normalized signals on Affymetrix expression microarray (FB7-7 *vs* FB28-7). (B) Expression ratio values are averaged along the chromosome. Here, red circle plot indicates average value in 2-Mb windows.
(PDF)

Figure S4 *Zbtb38* mRNA expression is demonstrably associated with its chromosomal copy number. (A) Array-CGH profiles of two RCC tumors harboring amplification over *Zbtb38* locus on chromosome 8. (B) Expression analysis of *Zbtb38* on 13 RCC tumors by real-time PCR. The values of the *y*-axis indicate the relative mRNA expression level compared to an average of those in normal kidneys of three control rats.
(PDF)

Figure S5 Array-CGH profiles of three hereditary (Eker rat) renal tumors. Red lines show log2 ratios of estimated copy number over inferred cancer ploidy versus genomic position for all the CGH microarray probes.
(PDF)

Table S1 List of genes completely deleted in more than two RCC tumors.
(XLS)

Table S2 List of genes amplified in more than two RCC tumors.
(XLS)

Methods S1 Supplementary methods.
(DOC)

Author Contributions

Conceived and designed the experiments: SA ST. Performed the experiments: SA YY HO YTL MI KA MO LJ H. Nagai HM EA. Analyzed the data: SA YO TT ST. Contributed reagents/materials/analysis tools: YS YK OH H. Nakagama. Wrote the paper: SA ST. Designed the software used in analysis: SA.

References

1. Weinberg RA (2007) The biology of cancer. New York: Garland Science, Tailor & Francis Group, LLC.
2. Klijn C, Holstege H, de Ridder J, Liu X, Reinders M, et al. (2008) Identification of cancer genes using a statistical framework for multiexperiment analysis of nondiscretized array CGH data. Nucleic Acids Res 36: e13.
3. Parsons DW, Jones S, Zhang X, Lin JC, Leary RJ, et al. (2008) An integrated genomic analysis of human glioblastoma multiforme. Science 321: 1807–1812.
4. Pfeifer GP, Hainaut P (2011) Next-generation sequencing: emerging lessons on the origins of human cancer. Curr Opin Oncol 23: 62–68.
5. Toyokuni S (1999) Reactive oxygen species-induced molecular damage and its applicaton in pathology. PatholInt 49: 91–102.
6. Halliwell B, Gutteridge JMC (2007) Free radicals in biology and medicine. New York: Oxford University Press.
7. Toyokuni S (1996) Iron-induced carcinogenesis: the role of redox regulation. Free Radic Biol Med 20: 553–566.
8. Toyokuni S (2009) Role of iron in carcinogenesis: Cancer as a ferrotoxic disease. Cancer Sci 100: 9–16.
9. Fenton HJH (1894) Oxidation of tartaric acid in presence of iron. J Chem Soc 65: 899–910.
10. Toyokuni S, Sagripanti JL (1992) Iron-mediated DNA damage: sensitive detection of DNA strand breakage catalyzed by iron. J Inorg Biochem 47: 241–248.
11. Ebina Y, Okada S, Hamazaki S, Ogino F, Li JL, et al. (1986) Nephrotoxicity and renal cell carcinoma after use of iron- and aluminum- nitrilotriacetate complexes in rats. J Natl Cancer Inst 76: 107–113.
12. Li JL, Okada S, Hamazaki S, Ebina Y, Midorikawa O (1987) Subacute nephrotoxicity and induction of renal cell carcinoma in mice treated with ferric nitrilotriacetate. Cancer Res 47: 1867–1869.
13. Toyokuni S, Mori T, Dizdaroglu M (1994) DNA base modifications in renal chromatin of Wistar rats treated with a renal carcinogen, ferric nitrilotriacetate. Int J Cancer 57: 123–128.
14. Toyokuni S, Tanaka T, Hattori Y, Nishiyama Y, Ochi H, et al. (1997) Quantitative immunohistochemical determination of 8-hydroxy-2′-deoxyguanosine by a monoclonal antibody N45.1: its application to ferric nitrilotriacetate-induced renal carcinogenesis model. Lab Invest 76: 365–374.
15. Toyokuni S, Uchida K, Okamoto K, Hattori-Nakakuki Y, Hiai H, et al. (1994) Formation of 4-hydroxy-2-nonenal-modified proteins in the renal proximal tubules of rats treated with a renal carcinogen, ferric nitrilotriacetate. Proc Natl Acad Sci USA 91: 2616–2620.
16. Toyokuni S, Luo XP, Tanaka T, Uchida K, Hiai H, et al. (1997) Induction of a wide range of C_{2-12} aldehydes and C_{7-12} acyloins in the kidney of Wistar rats after treatment with a renal carcinogen, ferric nitrilotriacetate. Free Radic Biol Med 22: 1019–1027.
17. Gutteridge J, Rowley D, Halliwell B (1981) Superoxide-dependent formation of hydroxyl radicals in the presence of iron salts. Detection of 'free' iron in biological systems by using bleomycin-dependent degradation of DNA. Biochem J 199: p263–265.
18. Sasaki K, Ikuta K, Tanaka H, Ohtake T, Torimoto Y, et al. (2011) Improved quantification for non-transferrin-bound iron measurement using high-performance liquid chromatography by reducing iron contamination. Mol Med Report 4: 913–918.
19. Tanaka T, Iwasa Y, Kondo S, Hiai H, Toyokuni S (1999) High incidence of allelic loss on chromosome 5 and inactivation of $p15^{INK4B}$ and $p16^{INK4A}$ tumor suppressor genes in oxystress-induced renal cell carcinoma of rats. Oncogene 18: 3793–3797.
20. Toyokuni S, Akatsuka S (2006) What has been learned from the studies of oxidative stress-induced carcinogenesis: Proposal of the concept of oxygenomics. J Clin Biochem Nutr 39: 3–10.
21. Kallioniemi A, Kallioniemi OP, Sudar D, Rutovitz D, Gray JW, et al. (1992) Comparative genomic hybridization for molecular cytogenetic analysis of solid tumors. Science 258: 818–821.
22. Macconaill LE, Van Hummelen P, Meyerson M, Hahn WC (2011) Clinical implementation of comprehensive strategies to characterize cancer genomes: opportunities and challenges. Cancer Discov 1: 297.
23. Negrini S, Gorgoulis VG, Halazonetis TD (2011) Genomic instability–an evolving hallmark of cancer. Nat Rev Mol Cell Biol 11: 220–228.
24. Adamovic T, McAllister D, Guryev V, Wang X, Andrae JW, et al. (2009) Microalterations of inherently unstable genomic regions in rat mammary carcinomas as revealed by long oligonucleotide array-based comparative genomic hybridization. Cancer Res 69: 5159–5167.
25. Femia AP, Luceri C, Toti S, Giannini A, Dolara P, et al. (2010) Gene expression profile and genomic alterations in colonic tumours induced by 1,2-dimethylhydrazine (DMH) in rats. BMC Cancer 10: 194.
26. Takabatake T, Fujikawa K, Tanaka S, Hirouchi T, Nakamura M, et al. (2006) Array-CGH analyses of murine malignant lymphomas: genomic clues to understanding the effects of chronic exposure to low-dose-rate gamma rays on lymphomagenesis. Radiat Res 166: 61–72.
27. Herzog CR, Desai D, Amin S (2006) Array CGH analysis reveals chromosomal aberrations in mouse lung adenocarcinomas induced by the human lung carcinogen 4-(methylnitrosamino)-1-(3-pyridyl)-1-butanone. Biochem Biophys Res Commun 341: 856–863.
28. Maser R, Choudhury B, Campbell P, Feng B, Wong K, et al. (2007) Chromosomally unstable mouse tumours have genomic alterations similar to diverse human cancers. Nature 447: 966–971.
29. Loeb LA, Bielas JH, Beckman RA (2008) Cancers exhibit a mutator phenotype: clinical implications. Cancer Res 68: 3551–3557.
30. Hisada M, Garber JE, Fung CY, Fraumeni JF, Li FP (1998) Multiple primary cancers in families with Li-Fraumeni syndrome. J Natl Cancer Inst 90: 606–611.
31. Gruis NA, van der Velden PA, Sandkuijl LA, Prins DE, Weaver-Feldhaus J, et al. (1995) Homozygotes for CDKN2 (p16) germline mutation in Dutch familial melanoma kindreds. Nat Genet 10: 351–353.
32. Kobayashi T, Hirayama Y, Kobayashi E, Kubo Y, Hino O (1995) A germline insertion in the tuberous sclerosis (Tsc2) gene give rise to the Eker rat model of dominantly inherited cancer. Nature Genet 9: 70–74.
33. Hino O (2004) Multistep renal carcinogenesis in the Eker (Tsc 2 gene mutant) rat model. Curr Mol Med 4: 807–811.
34. Yeung RS (2004) Lessons from the Eker rat model: from cage to bedside. Curr Mol Med 4: 799–806.
35. Huang X (2003) Iron overload and its association with cancer risk in humans: evidence for iron as a carcinogenic metal. Mutat Res 533: 153–171.
36. Hiroyasu M, Ozeki M, Kohda H, Echizenya M, Tanaka T, et al. (2002) Specific allelic loss of p16 (INK4A) tumor suppressor gene after weeks of iron-mediated oxidative damage during rat renal carcinogenesis. Am J Pathol 160: 419–424.
37. Toyokuni S, Okada S, Hamazaki S, Minamiyama Y, Yamada Y, et al. (1990) Combined histochemical and biochemical analysis of sex hormone dependence of ferric nitrilotriacetate-induced renal lipid peroxidation in ddY mice. Cancer Res 50: 5574–5580.
38. Zhang D, Okada S, Yu Y, Zheng P, Yamaguchi R, et al. (1997) Vitamin E inhibits apoptosis, DNA modification, and cancer incidence induced by iron-mediated peroxidation in Wistar rat kidney. Cancer Res 57: 2410–2414.
39. Torres EM, Williams BR, Tang YC, Amon A (2010) Thoughts on aneuploidy. Cold Spring Harb Symp Quant Biol 75: 445–451.
40. Torres EM, Williams BR, Amon A (2008) Aneuploidy: cells losing their balance. Genetics 179: 737–746.
41. Toyokuni S (2009) Mechanisms of asbestos-induced carcinogenesis. Nagoya J Med Sci 71: 1–10.

42. Hu Q, Akatsuka S, Yamashita Y, Ohara H, Nagai H, et al. (2010) Homozygous deletion of *CDKN2A/2B* is a hallmark of iron-induced high-grade rat mesothelioma. Lab Invest 90: 360–373.
43. Jean D, Thomas E, Manie E, Renier A, de Reynies A, et al. (2011) Syntenic relationships between genomic profiles of fiber-induced murine and human malignant mesothelioma. Am J Pathol 178: 881–894.
44. Nagai H, Okazaki Y, Hwu C, Misawa N, Yamashita Y, et al. (2011) Diameter of multi-walled carbon nanotubes is a critical factor in mesothelial injury and subsequent carcinogenesis. Proc Natl Acad Sci USA.
45. Cheng J, Jhanwar S, Klein W, Bell D, Lee W, et al. (1994) p16 alterations and deletion mapping of 9p21-p22 in malignant mesothelioma. Cancer Res 54: 5547–5551.
46. Xio S, Li D, Vijg J, Sugarbaker D, Corson J, et al. (1995) Codeletion of *p15* and *p16* in primary malignant mesothelioma. Oncogene 11: p511–515.
47. Romagosa C, Simonetti S, Lopez-Vicente L, Mazo A, Lleonart ME, et al. (2011) p16(Ink4a) overexpression in cancer: a tumor suppressor gene associated with senescence and high-grade tumors. Oncogene 30: 2087–2097.
48. Evangelou K, Bramis J, Peros I, Zacharatos P, Dasiou-Plakida D, et al. (2004) Electron microscopy evidence that cytoplasmic localization of the p16(INK4A) "nuclear" cyclin-dependent kinase inhibitor (CKI) in tumor cells is specific and not an artifact. A study in non-small cell lung carcinomas. Biotech Histochem 79: 5–10.
49. Reuschenbach M, Waterboer T, Wallin KL, Einenkel J, Dillner J, et al. (2008) Characterization of humoral immune responses against p16, p53, HPV16 E6 and HPV16 E7 in patients with HPV-associated cancers. Int J Cancer 123: 2626–2631.
50. Wullich B, Sattler HP, Fischer U, Meese E (1994) Two independent amplification events on chromosome 7 in glioma: amplification of the epidermal growth factor receptor gene and amplification of the oncogene MET. Anticancer Res 14: 577–579.
51. Campbell JM, Lockwood WW, Buys TP, Chari R, Coe BP, et al. (2008) Integrative genomic and gene expression analysis of chromosome 7 identified novel oncogene loci in non-small cell lung cancer. Genome 51: 1032–1039.
52. Birchmeier C, Birchmeier W, Gherardi E, Vande Woude GF (2003) Met, metastasis, motility and more. Nat Rev Mol Cell Biol 4: 915–925.
53. Filion GJ, Zhenilo S, Salozhin S, Yamada D, Prokhortchouk E, et al. (2006) A family of human zinc finger proteins that bind methylated DNA and repress transcription. Mol Cell Biol 26: 169–181.
54. Oikawa Y, Matsuda E, Nishii T, Ishida Y, Kawaichi M (2008) Down-regulation of CIBZ, a novel substrate of caspase-3, induces apoptosis. J Biol Chem 283: 14242–14247.
55. Hellman A, Zlotorynski E, Scherer SW, Cheung J, Vincent JB, et al. (2002) A role for common fragile site induction in amplification of human oncogenes. Cancer Cell 1: 89–97.
56. Albertson DG (2006) Gene amplification in cancer. Trends Genet 22: 447–455.
57. Martinez AC, van Wely KH (2010) Are aneuploidy and chromosome breakage caused by a CINgle mechanism? Cell Cycle 9: 2275–2280.
58. Wiechen K, Diatchenko L, Agoulnik A, Scharff KM, Schober H, et al. (2001) Caveolin-1 is down-regulated in human ovarian carcinoma and acts as a candidate tumor suppressor gene. Am J Pathol 159: 1635–1643.
59. Wiechen K, Sers C, Agoulnik A, Arlt K, Dietel M, et al. (2001) Down-regulation of caveolin-1, a candidate tumor suppressor gene, in sarcomas. Am J Pathol 158: 833–839.
60. Pal S, Vishwanath SN, Erdjument-Bromage H, Tempst P, Sif S (2004) Human SWI/SNF-associated PRMT5 methylates histone H3 arginine 8 and negatively regulates expression of ST7 and NM23 tumor suppressor genes. Mol Cell Biol 24: 9630–9645.
61. Nagai H, Ishihara T, Lee WH, Ohara H, Okazaki Y, et al. (2011) Asbestos surface provides a niche for oxidative modification. Cancer Sci 102: 2118–2125.
62. Nishiyama Y, Suwa H, Okamoto K, Fukumoto M, Hiai H, et al. (1995) Low incidence of point mutations in *H-*, *K-* and *N-ras* oncogenes and *p53* tumor suppressor gene in renal cell carcinoma and peritoneal mesothelioma of Wistar rats induced by ferric nitrilotriacetate. Jpn J Cancer Res 86: 1150–1158.
63. Tanaka T, Akatsuka S, Ozeki M, Shirase T, Hiai H, et al. (2004) Redox regulation of annexin 2 and its implications for oxidative stess-induced renal carcinogenesis and metastasis. Oncogene 23: 3980–3989.
64. Liu Y-T, Shang D-G, Akatsuka S, Ohara H, Dutta KK, et al. (2007) Chronic oxidative stress causes amplification and overexpresson of *ptprz1* protein tyrosine phosphatase to activate β-catenin pathway. Am J Pathol 171: 1978–1988.
65. Olshen AB, Venkatraman ES, Lucito R, Wigler M (2004) Circular binary segmentation for the analysis of array-based DNA copy number data. Biostatistics 5: 557–572.
66. Wiedemeyer R, Brennan C, Heffernan TP, Xiao Y, Mahoney J, et al. (2008) Feedback circuit among INK4 tumor suppressors constrains human glioblastoma development. Cancer Cell 13: 355–364.
67. Murakami H, Mizuno T, Taniguchi T, Fujii M, Ishiguro F, et al. (2011) LATS2 is a tumor suppressor gene of malignant mesothelioma. Cancer Res 71: 873–883.
68. Arai E, Ushijima S, Tsuda H, Fujimoto H, Hosoda F, et al. (2008) Genetic clustering of clear cell renal cell carcinoma based on array-comparative genomic hybridization: its association with DNA methylation alteration and patient outcome. Clin Cancer Res 14: 5531–5539.

Journal of Pathology
J Pathol 2012; **228:** 366–377
Published online 2 August 2012 in Wiley Online Library
(wileyonlinelibrary.com) DOI: 10.1002/path.4075

ORIGINAL PAPER

Iron overload signature in chrysotile-induced malignant mesothelioma

Li Jiang,[1] Shinya Akatsuka,[1] Hirotaka Nagai,[1,2] Shan-Hwu Chew,[1] Hiroki Ohara,[1,2] Yasumasa Okazaki,[1] Yoriko Yamashita,[1] Yutaka Yoshikawa,[3] Hiroyuki Yasui,[3] Katsuya Ikuta,[4] Katsunori Sasaki,[5] Yutaka Kohgo,[4] Seishiro Hirano,[6] Yasushi Shinohara,[7] Norihiko Kohyama,[8] Takashi Takahashi[9] and Shinya Toyokuni[1]*

[1] *Department of Pathology and Biological Responses, Nagoya University Graduate School of Medicine, 65 Tsurumai-cho, Showa-ku, Nagoya 466-8550, Japan*
[2] *Department of Pathology and Biology of Diseases, Graduate School of Medicine, Kyoto University, Yoshida-Konoe-cho, Sakyo-ku, Kyoto 606-8501, Japan*
[3] *Division of Analytical and Physical Chemistry, Department of Analytical and Bioinorganic Chemistry, Kyoto Pharmaceutical University, Kyoto, 607-8414, Japan*
[4] *Division of Gastroenterology and Hematology/Oncology, Department of Medicine, Asahikawa Medical University, Asahikawa 078-8510, Japan*
[5] *Department of Gastrointestinal Immunology and Regenerative Medicine, Asahikawa Medical University, Asahikawa 078-8510, Japan*
[6] *Research Center for Environmental Risk, National Institute for Environmental Studies, 16-2 Onogawa, Tsukuba 305-8506, Japan*
[7] *Work Environment Research Group, National Institute of Occupational Health and Safety, 6-21-1 Nagao, Tama-ku, Kawasaki 214-8585, Japan*
[8] *National Science Laboratory, Faculty of Economics, Toyo University, 5-28-20, Hakusan, Bunkyo-ku, Tokyo 112-8606, Japan*
[9] *Department of Tumor Biology, Nagoya University Graduate School of Medicine, 65 Tsurumai-cho, Showa-ku, Nagoya 466-8550, Japan*

**Correspondence to: Professor Shinya Toyokuni, Department of Pathology and Biological Responses, Nagoya University Graduate School of Medicine, 65 Tsurumai-cho, Showa-ku, Nagoya, Japan. e-mail: toyokuni@med.nagoya-u.ac.jp*

Abstract

Exposure to asbestos is a risk for malignant mesothelioma (MM) in humans. Among the commercially used types of asbestos (chrysotile, crocidolite, and amosite), the carcinogenicity of chrysotile is not fully appreciated. Here, we show that all three asbestos types similarly induced MM in the rat peritoneal cavity and that chrysotile caused the earliest mesothelioma development with a high fraction of sarcomatoid histology. The pathogenesis of chrysotile-induced mesothelial carcinogenesis was closely associated with iron overload: repeated administration of an iron chelator, nitrilotriacetic acid, which promotes the Fenton reaction, significantly reduced the period required for carcinogenesis; massive iron deposition was found in the peritoneal organs with high serum ferritin; and homozygous deletion of the *CDKN2A/2B/ARF* tumour suppressor genes, the most frequent genomic alteration in human MM and in iron-induced rodent carcinogenesis, was observed in 92.6% of the cases studied with array-based comparative genomic hybridization. The induced rat MM cells revealed high expression of mesoderm-specific transcription factors, *Dlx5* and *Hand1*, and showed an iron regulatory profile of active iron uptake and utilization. These data indicate that chrysotile is a strong carcinogen when exposed to mesothelia, acting through the induction of local iron overload. Therefore, an intervention to remove local excess iron might be a strategy to prevent MM after asbestos exposure.

Keywords: asbestos; malignant mesothelioma; iron; array-based comparative genomic hybridization; *CDKN2A/2B*; *ARF*

Received 3 April 2012; Revised 28 June 2012; Accepted 11 July 2012

No conflicts of interest were declared.

Introduction

Natural fibrous minerals have been unexpected human carcinogens. Asbestos was valued as a miraculous stone because of heat-, acid-, and friction-resistance with economical merits, and thus was used from the ancient Egyptian era until the present century for wide industrial applications. However, in the 1960s, epidemiologists noticed the association between asbestos and malignant mesothelioma (MM) [1], which is a highly aggressive tumour when diagnosed, resistant to the currently available therapeutic modalities [2,3]. Due to a long incubation period, the expected peak year of MM in Japan is 2025, and over 100 000 people will suffer from MM in the coming 40 years [4]. This prompted us to elucidate the carcinogenic mechanism of asbestos-induced MM to discover clues for MM prevention. Lung cancer is also associated with asbestos exposure, but the situation is more complex because asbestos holds a synergistic effect with the carcinogenicity of tobacco [5].

In 1987, the International Agency for Research on Cancer defined all types of asbestos as a definite carcinogen to humans [1], but the appreciation of this declaration is quite different among countries [6]. Three kinds of asbestos fibres, chrysotile (white

asbestos), crocidolite (blue asbestos), and amosite (brown asbestos), have been used commercially, but the asbestos most frequently used has unequivocally been chrysotile [7]. Most Asian countries including China and India, and Russia, have not legally banned any type of asbestos. In Japan, the use of any type of asbestos was banned in September 2006 after the 'Kubota shock' in June 2005 [8]. Canada still maintains chrysotile mine operations [9].

Thus far, the notion that crocidolite and amosite, with their high iron contents (28.5% and 27.3%, respectively) [10], are far more carcinogenic than chrysotile (0.7%) has predominated [1]. However, controversies still exist [7]. In the present study, we used rat intraperitoneal experiments to evaluate the difference among the three asbestos types regarding carcinogenicity and the induced genomic alterations in MMs. The use of the peritoneal cavity is justified in that the interaction of asbestos and mesothelial cells is direct and maximal, presumably requiring less time for carcinogenesis [1], although respiratory factors have to be considered separately. Reportedly, inhalation of asbestos induces MM in a small percentage of animals [7], whereas intrapleural injection of asbestos takes a long time (mean survival ~2 years) for MM to develop, albeit with a high rate (25–69%) [1,11]. Here, we report that the progression of the disease (lethal MM) induced by chrysotile was the fastest, with similar genomic alterations shared by the three commercially used asbestos types.

Materials and methods

Measurements of asbestos fibres

Asbestos fibres were suspended and diluted in H_2O containing 1% NP40S (Tergitol; Sigma Aldrich, St Louis, MO, USA), followed by sonication for 30 min. We used a haemocytometer and microscopy to count the number and to measure the length of asbestos fibres for estimation by the use of Nikon ACT-1 software.

Carcinogenesis study using an animal model

The Animal Experiment Committee of the Graduate School of Medicine, Kyoto University and the Nagoya University Graduate School of Medicine approved these experiments. A suspension of UICC standard asbestos (chrysotile A, crocidolite, and amosite) in saline was prepared as described previously [12]. F_1 hybrid rats produced by crossing over between female Fischer 344 and male Brown-Norway rats (Charles River Japan, Yokohama, Japan) were used under specific pathogen-free conditions. A total of 141 F_1 rats were divided into the following five groups: untreated control ($N = 38$); chrysotile-treated ($N = 28$); crocidolite-treated ($N = 41$); amosite-treated ($N = 28$); and tangled multi-walled carbon nanotube (CNT; $N = 6$; Showa Denko, diameter $\phi = \sim 15$ nm). The characteristics of this nanotube are described elsewhere [13]. A total of 10 mg asbestos/CNT per rat was injected intraperitoneally with three injections (Figure 2a) when the F_1 rats reached 6 weeks of age (Supplementary Table 1). Some of the asbestos-treated rats were then given 80 mg/kg nitrilotriacetate (NTA) to enhance iron-catalysed Fenton reaction through separate intraperitoneal injections once a week for 16 weeks as described previously [14,15]. The animals were kept under close observation. When animals displayed massive ascites or distress, they were sacrificed. Control groups of rats, untreated or exposed to CNT, were sacrificed on day 940 and 742, respectively (Figure 2c). The rats were dissected and tissue samples were either fixed in phosphate-buffered 10% formalin for subsequent histological and immunohistochemical analyses, or snap-frozen in liquid nitrogen and stored at $-80\,^{\circ}C$ until use. For a sub-acute study, the rats were subjected to a single intraperitoneal injection of 5 mg of chrysotile ($N = 6$), crocidolite ($N = 6$), and amosite ($N = 6$), respectively. Control rats ($N = 3$) were injected with saline. After 2 weeks, half of the asbestos-treated rats were injected intraperitoneally with NTA (80 mg/kg) and sacrificed 24 h afterwards. Rats injected with NTA without prior exposure to asbestos were also included as a control ($N = 3$).

Collection of normal control mesothelial cells from rats

Age-matched male rats were dissected and control mesothelial cells were collected as previously described [16].

Materials

All of the chemicals used were of analytical quality.

Array-based comparative genomic hybridization (aCGH)

We performed aCGH using Rat Genome CGH Microarray 244A (G4435A; Agilent Technologies, Santa Clara, CA, USA) according to the manufacturer's protocol. DNA from MM samples was labelled with Cy-5, while DNA from normal kidney, which was used as a reference, was labelled with Cy-3 for each array. The data obtained were analysed with Genomic Workbench Standard Edition 5.0 (Agilent Technologies). Prior to hierarchical clustering based on the aCGH profiles, statistically significant regions of copy number aberration were determined by the ADM-2 algorithm according to the sensitivity threshold at 10.0. The clustering procedure was conducted using the Pearson correlation similarity measure and complete linkage algorithm. We statistically evaluated the magnitude of chromosomal aberrations in the genome of each tumour as follows: an average of squares of $\log_2$ ratios between two-colour

hybridization signals for all the probes on the microarray was compared among each group by using the unpaired t-test.

Array-based CGH data may be found under the following GEO accession: GSE36577.

Genome copy analysis

Genomic DNA was extracted by using the DNeasy Blood and Tissue Kit (QIAGEN GmbH, Hilden, Germany). Quantitative PCR analysis was performed using the Platinum SYBR Green qPCR SuperMix UDG Kit (Invitrogen, Carlsbad, CA, USA) and Real-time PCR System 7300 (Applied Biosystems, Foster City, CA, USA). Primer sequences are described in Supplementary Table 2.

Fluorescence *in situ* hybridization (FISH)

Bacterial artificial chromosome clones (CH230-163D24) were purchased from http://bacpac.chori.org/ for *CDKN2A/2B*. Fluorescent probes were labelled by incorporating Green-dUTP (Vysis; Abbott Laboratories, Abbott Park, IL, USA) into newly synthesized DNA via the Nick Translation Kit (Vysis). Fluorescence *in situ* hybridization was performed using the probes, the Paraffin Pretreatment Kit, and LSI/WCP Hybridization Buffer (Vysis) according to the manufacturer's protocol. Briefly, paraffin sections were treated with protease, and after denaturation, the probes were hybridized to nuclear DNA, counterstained with DAPI, and visualized using a fluorescence microscope.

Reverse transcription and real-time PCR

Total RNA was isolated from tissue samples using the RNeasy Mini Kit (QIAGEN). The isolated total RNA was then treated with DNase I (Invitrogen Life Technologies) to digest remnant genomic DNA. cDNA was synthesized from 4 μg of total RNA using the First-Strand cDNA Synthesis Kit (GE Healthcare Offices, Little Chalfont, Buckinghamshire, UK) with random primers. For real-time quantitative PCR analysis, the Platinum SYBR Green qPCR SuperMix UDG Kit (Invitrogen) and Real-time PCR System 7300 (Applied Biosystems) were used. Each target gene was assayed in triplicate. Primer sequences are described in Supplementary Table 2.

Antibodies

Anti-podoplanin rabbit polyclonal antibody (KS-17) was from Sigma. Anti-multi-cytokeratin mouse monoclonal antibody (RTU-AE1/AE3) was from Novocastra (Newcastle, UK). Anti-desmin mouse monoclonal antibody (clone D33) was from DAKO (Carpinteria, CA, USA). Anti-calretinin rabbit monoclonal antibody (clone SP13) was from Abcam (Cambridge, MA, USA). Anti-S-100 polyclonal antibody (clone D33) was from DAKO. Anti-C-ERC/mesothelin monoclonal antibody was from IBL (Takasaki, Gunma, Japan). Anti-8-hydroxy-2′-deoxyguanosine (8-OHdG) mouse monoclonal antibody N45.1 [17] and anti-rat DMT1 rabbit polyclonal antibody [18] were used.

Western blot analysis

Protein lysates were prepared by homogenizing the tissue samples in RIPA lysis buffer containing 0.2 mmol/l sodium orthovanadate (Na_3VO_4), 50 mmol/l sodium fluoride (NaF), 1 mmol/l dithiothreitol, and 5.7 mg/ml aprotinin. Western blot was performed as described previously [19].

Tissue array, histology, and immunohistochemical analysis

We randomly selected 21 cases of epithelioid mesothelioma (EM; seven cases each from the chrysotile, crocidolite, and amosite groups) and 21 cases of sarcomatoid mesothelioma (SM; seven cases each from the chrysotile, crocidolite, and amosite groups) for tissue array preparation, and included liver, spleen, and kidney specimens in each tissue array. Representative areas from tissue specimens were chosen and cores of 3 mm diameter were punched out from the paraffin blocks with a precision instrument (Tissue Microprocessor; Azumaya, Tokyo, Japan). Cores of 24 (6×4 array) in a group were embedded in a paraffin block. Tissue sections of 3 μm thickness were then subjected to either haematoxylin and eosin staining or Perl's iron staining. For immunohistochemical analysis, the avidin–biotin complex method with peroxidase was used as described previously [17]. Immunostaining results were mostly uniform in distribution and were thus evaluated by two registered pathologists (YO and ST) as positive (+), weakly positive (weak +) or negative.

Serum ferritin and N-ERC/mesothelin assay

Commercial kits were used to measure rat serum ferritin (Mitsubishi Chemical Safety Institute Ltd, Uto, Kumamoto, Japan) and mesothelin (Immuno-Biological Laboratories Co, Ltd, Takasaki, Gunma, Japan) [20].

Measurement of iron content

Iron concentration was determined by inductively coupled plasma-mass spectrometry using a Shimadzu ICPM-8500 (Shimadzu, Kyoto, Japan) as described previously [13].

Measurement of non-transferrin-bound iron (NTBI)

Serum NTBI concentrations were measured as described previously [21].

Statistical analysis

Kaplan–Meier and other statistical analyses were performed using SPSS software. p values for Kaplan–Meier analysis were calculated by the log-rank test. Other analyses used were the unpaired t-test, modified